A

Cell	Mode	Karyotype
AT1OS	44(1),45(3), 46(44),47(2)	46,XY[10] 44,XY,-1,-6,add(12)(q24.1)[1] 45,XY,del(3)(q23),-6,del(14)(q32)[1] 45,XY,add(4)(p16),-16[1] 45,XY,add(11)(p15),-22[1] 46,XY,add(3)(p13),add(14)(q24)[1] 46,XY,t(3;15)(q23;p11.2)[1] 46,XY,add(11)(p11.1)[1] 46,XY,add(14)(q32)[1] 46,XY,add(2)(q31),+20[1] 46,XY,add(2)(q31),-16,+2mar[1]

B

Cell	Passage	Karyotype
ATiPS-262	P16	46,XY[19] / 45,XY,der(17;21)(q10;q10)[1]
ATiPS-263	P15	46,XY[20]
ATiPS-264	P15	46,XY[19] / 46,Y,add(X)(p22.1)[1]
ATiPS-024	P13	46,XY[20]

C

Cell	Passage	Karyotype
ATiPS-262	P41	46,XY[20]
ATiPS-263	P41	46,XY[20]
ATiPS-264	P41	46,XY[20]
ATiPS-024	P41	46,XY[20]

D

Cell	Passage	Karyotype
ATiPS-262	P76	46,XY[20]
ATiPS-263	P84	46,XY[20]
ATiPS-264	P81	46,XY[20]
ATiPS-024	P85	46,XY[20]

Figure 3 | Karyotypes of AT-iPS cells and their parental cells after long-term cultivation. (A). Karyotypic analysis of AT1OS parental cells. (B). Karyotypic analyses of AT-iPS cell clones at Passage 13–16. (C). Karyotypic analyses of AT-iPS cell clones at Passage 41. (D). Karyotypic analyses of AT-iPS cell clones at Passage 76–85. For karyotypic analysis, 20 cells were analyzed and the number of cells with the indicated karyotype was shown in brackets.

deletion in ATiPS-024 cells involved 2, 37, and 1 SNVs, respectively. These SNVs were removed from the count because the events were caused by large-scale structural mutations rather than single nucleotide substitutions. Furthermore, ambiguously called five SNVs that escaped from the filtering process were manually eliminated (Supplemental Table S2). The numbers of SNVs were 43, 48, 35, and 41 (167 SNVs in total) in ATiPS-262, ATiPS-263, ATiPS-264, and ATiPS-024 cells, respectively (Figure 4B, Supplemental Table S2). Importantly, the identified number of non-synonymous coding bases is larger than that of synonymous coding (Figure 4C). We estimated that 0.48 single nucleotide alterations had occurred per population doubling (PD) in the AT-iPS cells. Single nucleotide change patterns in the 4 AT-iPS cells were summarized in Figure 4D.

Detection of genomic mutation by the whole exome analysis. The whole exome analysis, in which our samples were compared to the hg19 reference sequence, also detected the homozygous mutation at a splice donor site of the *ATM* gene (chr11:108164206, IVS31 + 2T > A) (Supplemental Table S3). The mutation at the splice donor site is compatible with the truncated *ATM* mRNA that had a deletion of exon 31 (Figure 2A). The detection of this mutation confirms reliability of the whole exome analysis.

Sensitivity to irradiation in AT-iPS cells. AT patients and the cells derived from the patients show higher sensitivity to ionizing radiations and to radiomimetic drugs. Thus, we examined the radiosensitivity of AT-iPS cells, and compared it with that of MRC5-iPS cells (Figure 5A). Five minutes after irradiation at

Table 1 | Telomere length measurement for iPS cells

Cell	Metaphase No. of Metaphase Spreads Examined	Mean Values of Median TFI	Sample TFI/Control TFI	Telomere Length (kbp)
AT1OS	4	5187	0.598	4.13
ATiPS-262	8	16495	1.902	13.14
TIG-1	5	8671	1.000	6.91
ATiPS-264	12	17539	2.263	15.64
TIG-1	7	7751	1.000	6.91
ATiPS-024	14	17654	2.393	16.54
TIG-1	10	7378	1.000	6.91

Telomere length of TIG-1 cells at 34 population doublings is 6.91 kbp.
TFI: Telomere Fluorescence Intensity.

0.5 Gy, the phosphorylation of ATM increased in MRC5-iPS cells. In contrast, ATM protein was undetectable in the non-irradiated state, and was barely induced and phosphorylated in AT-iPS cells even after irradiation.

Two days after X-ray irradiation, cell number was measured in four independent AT-iPS cell clones and three MRC5-iPS cell clones to estimate growth retardation and cell survival (Figure 5B, Supplemental Figure S7A). All AT-iPS clones exhibited markedly lower survival rates than those of MRC5-iPS clones at all different doses examined. At the low dose of irradiation (0.5 Gy), cell growth curve profiles showed that AT-iPS cell growth decreased between day 5 and day 7 post-irradiation, but recovered their proliferation rate at day 8 (Figure 5C). AT-iPS cells exhibited higher sensitivity morphologically to irradiation, compared with MRC5-iPS cells

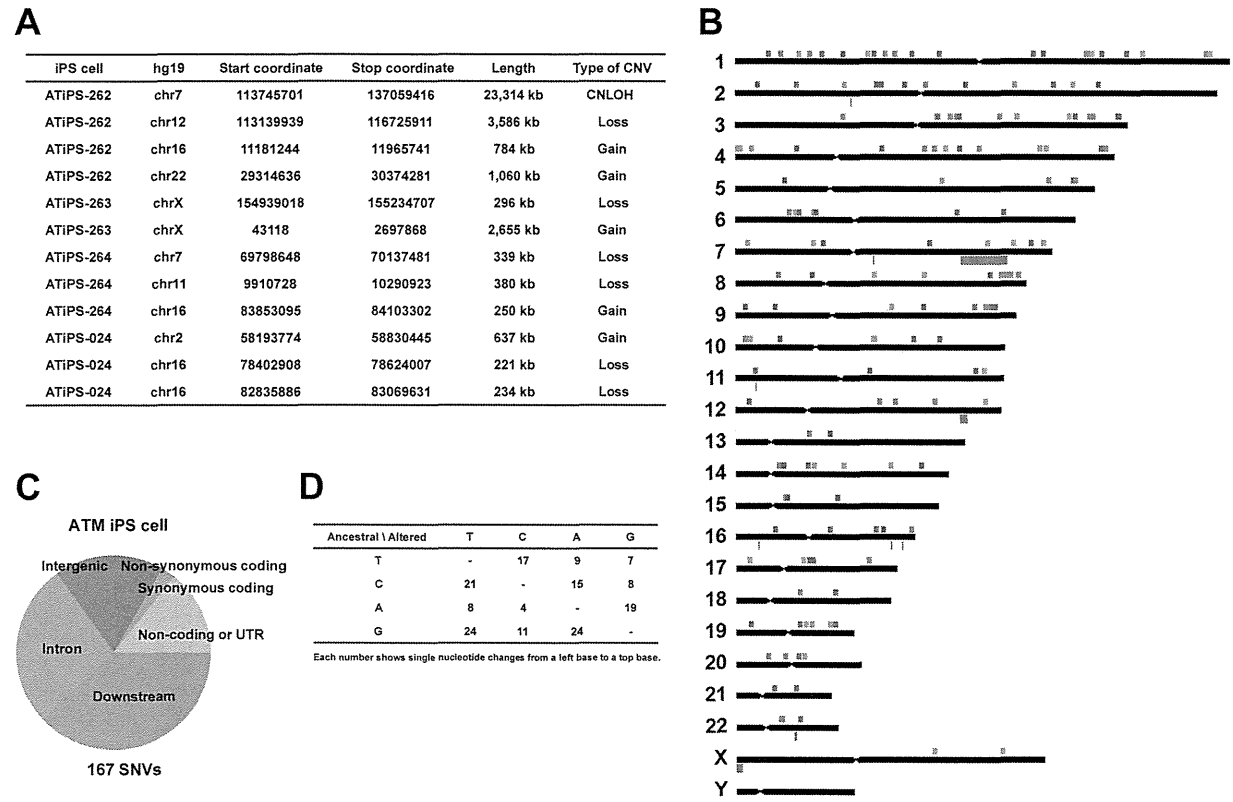

Figure 4 | Genomic alterations in AT-iPS cell cultivation. (A). Structural alterations identified by a comparison between parental AT1OS cells and AT-iPS cells. (B). Genome-wide distribution of SNVs identified in the AT-iPS cells. Filled squares above a chromosomal bar stand for genomic position of each SNV. Orange, yellowish green, green, and blue squares indicate alteration events occurred in the ATiPS-262, ATiPS-263, ATiPS-264, and ATiPS-024 iPS cells, respectively. A 23-Mb copy-neutral LOH region on chromosome 7 (ATiPS-262), a 3.6-Mb deletion on chromosome 12 (ATiPS-262), and a 0.23-Mb deletion on chromosome 16 (ATiPS-024) involved 2, 37, and 1 nucleotide mismatches detected during the course of our exome analysis, respectively. (C). Pie chart illustrating the ratio of protein-coding and non-coding sequences. Our exome analysis targeted 93,907,534 bases in the genome, and 30,331,579 bases within them are considered coding sequences, start or stop codons. Covering large part of non-coding sequences was one of features of the present exome study. Note that numbers of non-synonymous coding bases are larger than those of synonymous coding bases in the AT-iPS cells. Annotations were performed using SnpEff 3.1 (http://snpeff.sourceforge.net/SnpEff_manual.html). For example, if a variation was positioned within 5 kb from the 3′ end of a gene, it was annotated as "downstream." (D). Single nucleotide change patterns observed in AT-iPS cells.

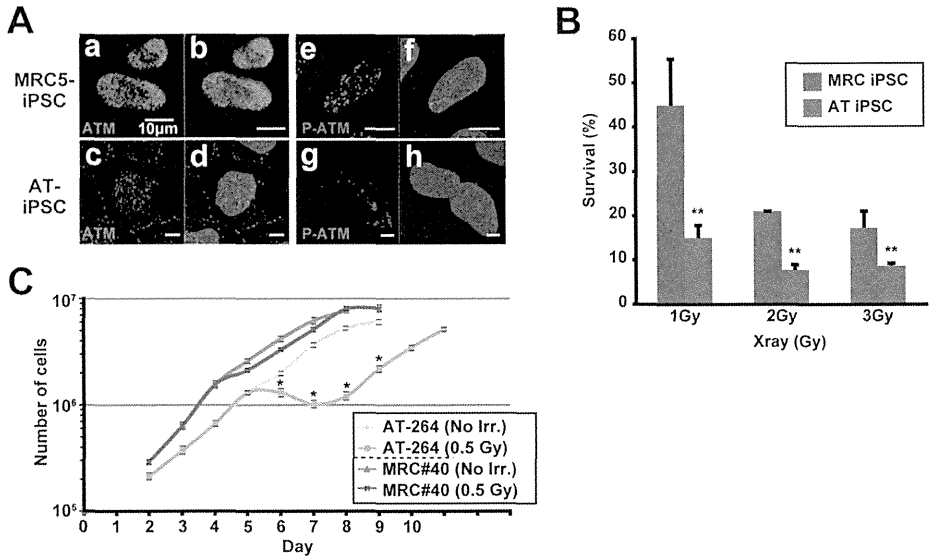

D

Cell	Passage	Irradiation (Gy)	Mode	Karyotype
MRCiPS#16	P59	0	46(50)	46,XY[20]
		0.5	46(48),47(2)	46,XY[19] 46,XY,chtb(14)(q24)[1]
		1.0	45(1),46(49)	46,XY[19] 45,XY,dic(2;2)(p23;P25)[1]
MRCiPS#25	P43	0	46(50)	46,XY[20]
		0.5	46(50)	46,XY[20]
		1.0	46(50)	46,XY[20]
MRCiPS#40	P62	0	46(50)	46,XY[20]
		0.5	46(50)	46,XY[20]
		1.0	46(50)	46,XY[20]
ATiPS-262	P76	0	46(50)	46,XY[20]
		0.5	46(50)	46,XY[20]
		1.0	46(50)	46,XY[20]
ATiPS-263	P84	0	46(50)	46,XY[20]
		0.5	46(50)	46,XY[20]
		1.0	46(50)	46,XY[20]
ATiPS-264	P81	0	46(50)	46,XY[20]
		0.5	46(50)	46,XY[20]
		1.0	44(1),46(48),49(1)	46,XY[17] 46,XY,t(18;19)(q12.2;p13.3)[1] 44,XY,qr(1;3)(p22;p21),-5,-9,chtb(9)(p22),chtb(16)(q11.1),-22,+2mar[1] 49,X,-Y,add(1)(q42),add(4)(q?25),chtb(8)(p21),-14,chtb(17)(p11.2),+5mar[1]
ATiPS-024	P85	0	46(50)	46,XY[20]
		0.5	46(50)	46,XY[18] 46,XY,chtb(17)(q?23) x 2[1] 46,XY,dic(1;2)(q44;p25),mar[1]
		1.0	46(50)	46,XY[20]

Figure 5 | Effect of X-ray irradiation on AT-iPS cells. (A). Immunocytochemistry of ATM (a and c: green) and phosphorylated ATM (e and g: red, labeled as P-ATM). AT-iPS (ATiPS-262) and MRC5-iPS (MRCiPS#16) cells were analyzed at 5 min after 0.5-Gy irradiation. (a), (b), (e) and (f): MRC5-iPS cells; (c), (d), (g) and (h): AT-iPS cells (ATiPS-262). (b) and (d): Merge of ATM and DAPI stain; (f) and (h): Merge of phosphorylated ATM and DAPI stain. (B). Dose effect of irradiation on AT-iPS cells (ATiPS-262, -263, -264, -024) and MRC5-iPS cells (MRCiPS#16, #25, #40). Frequencies of viable cells were calculated from the cell number on 2 days after irradiation at the indicated doses to estimate growth retardation and cell survival. Data for AT-iPS and MRC5-iPS cells were obtained from the quadruplicate and triplicate independent experiments, respectively. Nonirradiated cells were regarded as equal to 100%. Asterisks (**) denote statistically significant with $p < 0.01$ by student's t-test (1 Gy, $p = 1.2 \times 10^{-3}$; 2 Gy, $p = 5.1 \times 10^{-6}$; 3 Gy, $p = 2.8 \times 10^{-3}$). (C). Effect of irradiation on growth of AT-iPS and MRC5-iPS cells. iPS cells were irradiated at 0.5 Gy on Day 4. Cell number was calculated at the indicated days after cells (10^5) were seeded on Day 0. Non-irradiated (No Irr.) iPS cells were also shown for control. Asterisks (*) denote statistically significant between irradiated and nonirradiated cells with $p < 0.01$ by student's t-test (Day 6, $p = 3.2 \times 10^{-4}$; Day 7, $p = 6.1 \times 10^{-6}$; Day 8, $p = 3.8 \times 10^{-6}$; Day 9, $p = 9.9 \times 10^{-7}$). (D). Irradiation effect on karyotypes of AT-iPS cells. Mode: 50 cells were analyzed for chromosomal aneuploidy. Number of cells with each chromosomal number is shown in Parentheses. Karyotype: For karyotypic analysis, 20 cells were analyzed and the number of karyotype was shown in brackets.

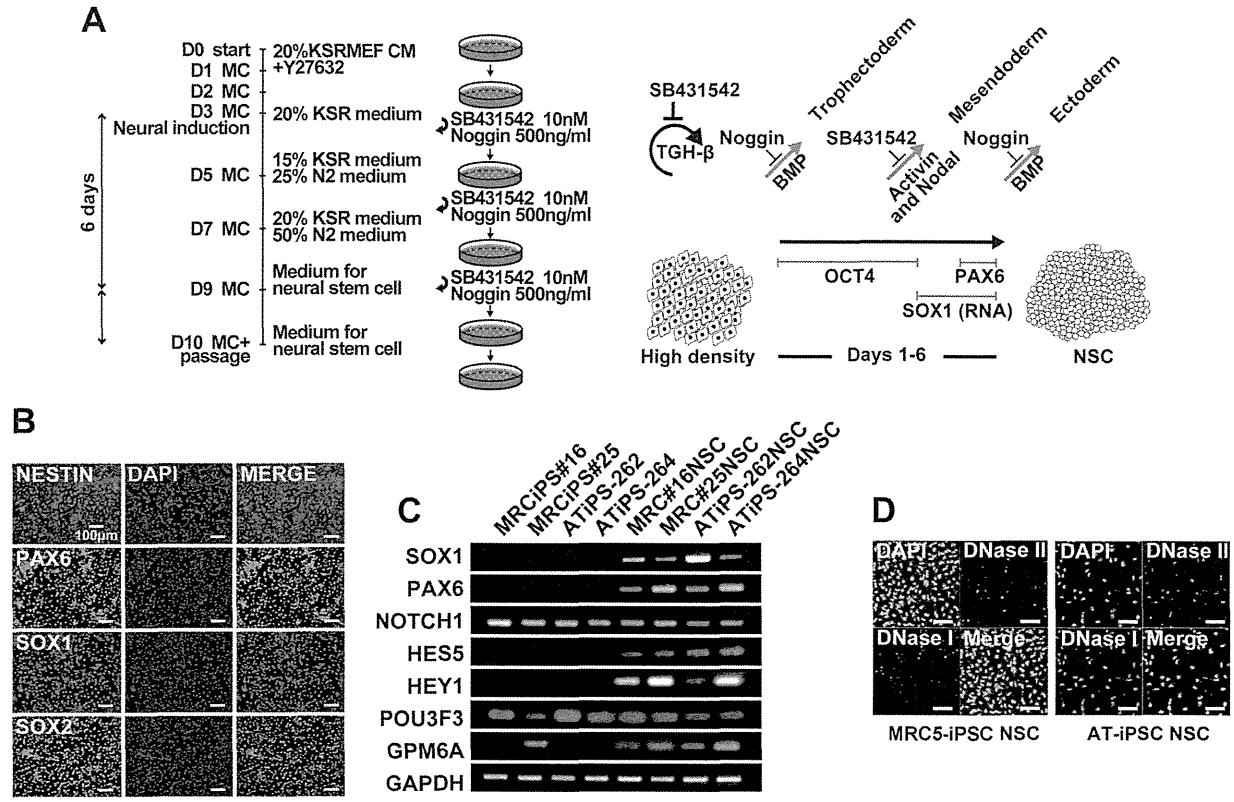

Figure 6 | Neural differentiation of AT-iPS cells. (A).Protocol for neural differentiation of AT-iPS cells. Neural differentiation of iPS cells was performed according to the standard protocol[37]. MC: Medium change. (B). Immunocytochemistry of AT-iPS cells (ATiPS-262). (C). RT-PCR analysis on AT-iPS cells (ATiPS-262, ATiPS-264) and MRC5-iPS cells (MRCiPS#16, MRCiPS#25) after neural differentiation. Primers are listed in Supplemental Table S1. (D). Apoptosis of AT-iPS cells after neural differentiation. Apoptosis was detected by the ApopTag ISOL Dual Fluorescence Apoptosis Detection Kit (DNase Types I & II) APT1000 (Millipore). Left panels: neural differentiation of MRC5-iPS cells (MRCiPS#25), right panels: neural differentiation of AT-iPS cells (ATiPS-262).

(Supplemental Figure S7B, C). These results indicate that AT-iPS cells have higher radiation sensitivity than the intact iPS cells when growth characteristics are considered.

Karyotypic analyses of AT-iPS cells and MRC5-iPS cells were performed after X-ray irradiation, and did not reveal any significant difference in the radiation sensitivity. Most cells analyzed showed an intact chromosomal pattern even after longer cultivation (ATiPS-264: Passage 81 and 20 months, ATiPS-024: Passage 86 and 22 months). Only low frequencies of chromosomal abnormalities such as chromosomal loss and amplification, deletion, and translocation were detected in AT-iPS cells; MRC5-iPS cells showed similar results (Figure 5D).

Neural differentiation of iPS cells. Since one of the most common symptoms in patients with ataxia telangiectasia is neural impairment, we investigated neural differentiation of AT-iPS cells (ATiPS-262 and -264) and MRC5-iPS cells (MRCiPS#16 and #25) (Figure 6A). AT-iPS cells exhibited neural phenotypes by morphological analysis, immunocytochemistry (Figure 6B), and RT-PCR analysis (Figure 6C, Supplemental Figure S8), and no significant difference between AT-iPS cells and MRC5-iPS cells were detected. However, apoptosis significantly increased after neural differentiation of AT-iPS cells, compared with MRC5-iPS cells (Figure 6D). We obtained consistent results from all iPS cells examined.

Discussion

Human pluripotent stem cells deficient for the ATM gene have successfully been generated in two ways: Disruption of the ATM gene in human ES cells by genetic manipulation with bacterial artificial chromosome and derivation of disease-specific iPS cells from patients with ataxia telangiectasia[11–13]. The ATM-deficient pluripotent stem cells serve as disease model cells for clarification of pathogenic mechanisms and for screening novel compounds to treat the disease. In this study, we generated iPS cells from fibroblasts (AT1OS) of a human AT patient, and compared them with those from a healthy donor. The AT-iPS cells exhibited the same proliferation activity as wild type-iPS cells (WT-iPS cells), a gene expression profile characteristic of pluripotent stem cells such as ES cells and WT-iPS cells, the capability to differentiate into all three germ layers, and hypersensitivity in growth characteristics to X-ray irradiation. Apoptosis could be induced upon neural differentiation of AT-iPS cells. These results indicate that the established cells kept both characteristics of pluripotent stem cells and *ATM*-deficient cells.

Though normal ATM function was not a prerequisite for the establishment and maintenance of iPS cells, the reprogramming efficiency of the fibroblasts derived from an AT patient was extremely low, suggesting indirect roles of ATM in the somatic reprogramming process. One of the major targets of ATM is p53[14], and ATM-dependent phosphorylation is directly responsible for p53 activation. ATM and p53 are two proteins that are believed to play a major role in maintaining the integrity of the genome. In spite of having the related function of maintaining the integrity of the genome, p53 is known to serve as a barrier in iPS cell generation. Genetic ablation or decreased amounts of p53 remarkably increases reprogramming efficiency in mouse and human somatic cells[15–19]. Thus, ATM and p53

appear to have opposite roles on the reprogramming of differentiated cells to pluripotent cells. ATM kinase phosphorylates a broad range of substrates, and is involved in a wider range of safeguard systems than p53, such as DNA repair, apoptosis, G1/S, intra-S checkpoint and G2/M checkpoints. Thus, p53-independent reprogramming processes may have a crucial need for some ATM functions, and other phosphatidyl-inositol 3-kinase like enzymes, such as ATR, may partially compensate the ATM-deficiency.

Alternatively, telomere damage may explain the low reprogramming efficiency found in AT-derived fibroblasts. Telomeres found at the ends of eukaryotic chromosomes prevent their erosion, facilitate the recruitment of telomere-binding factors and stop the activation of the DNA damage response pathways. In humans, *ATM* deficiency results in accelerated telomere loss, and T lymphocytes derived from AT-patients exhibit frequent telomeric fusions[20]. Mouse cells with short telomeres cannot be reprogrammed to iPS cells despite their normal proliferation rates, probably reflecting the existence of 'reprogramming barriers' that abort the reprogramming of cells with uncapped telomeres[21,22].

Unexpectedly, we found that AT-iPS cells did not show any chromosomal instability *in vitro*, i.e., maintenance of intact chromosomes was observed after 80 passages (560 days). Even after X-ray irradiation at low dose, the most of AT-iPS cells still maintained an intact karyotype. In contrast, the parental fibroblastic cell line, AT1OS, showed frequent chromosomal abnormalities, such as deletion, addition and translocation. However, the AT-iPS cells still exhibited hypersensitivity to X-ray irradiation in the growth profile, which are major characteristics of ATM-deficient cells. These results indicate that AT-iPS cells maintain the defective response to ionizing irradiation, but that the defects do not affect maintenance of intact chromosomes.

What are the causes of the differences in the chromosomal stability between AT-iPS cells and AT1OS cells, the source of AT-iPS cells? The major difference between iPS cells and somatic cells may be the ability to undergo unlimited self-renewal. Somatic cells usually have limited growth potential, gradually decline with advancing age, and finally fall into senescence. In contrast, pluripotent stem cells are characterized by unlimited self-renewal and the ability to generate differentiated functional cell types. One of the causes of immortality is the presence of a terminal DNA polymerase capable of synthesizing telomeres, and somatic cell mortality is the result of a progressive loss of the telomeric DNA because of the absence of the immortalizing polymerase. The function of telomerase in terminal DNA elongation is necessary in order to overcome the "end-replication problem" whereby conventional DNA polymerases cannot fully replicate linear DNAs[23]. Telomere erosion (by 50–100 bp per cellular division) limits the replicative capacity of the majority of somatic cells, which do not express active telomerase[24]. In humans, *ATM* deficiency results in accelerated telomere loss in somatic cells, and T lymphocytes derived from AT patients exhibit frequent chromosomal instability[20].

Response to oxidative stress may be one of the causes of the accelerated telomere loss. It has been suggested that somatic cells, such as fibroblasts and neuronal cells from AT patients are in a chronic state of oxidative stress, which could contribute to their enhanced telomere shortening[25]. ATM protein is suggested to have a role in the prevention or repair of oxidative damage to telomeric DNA, and enhanced sensitivity of telomeric DNA to oxidative damage in AT cells results in accelerated telomere shortening and chromosomal instability. Further study using telomerase inhibitors and anti-oxidants using the human AT-iPS cells may clarify the cause of the difference between somatic cells and iPS cells derived from AT patients.

The number of single-nucleotide mutations per cell genome was estimated from 22 human iPS cells by extensive exome analysis on protein-coding sequences[26]. The exome analysis on the AT-iPS cell lines from 17 to 27 passages after the establishment in this study included not only coding but also untranslated, non-coding RNA, and their adjacent regions, covering up to 93.9 Mb. The number of observed coding mutations during reprogramming was comparable or smaller in all the three lines than those reported by the preceding study[26], supporting a genetic stability of the AT-iPS cells.

AT is characterized by early onset progressive cerebellar ataxia, oculocutaneous telangiectasia, susceptibility to bronchopulmonary disease, and lymphoid tumors. The pathologic tissues are generally not easily accessible, resulting in a substantial disadvantage for medical and biological studies of the pathogenesis of the disease and for development of novel therapeutic interventions. Generation of *Atm*-deficient mice partially overcomes such difficulties. However, oculocutaneous telangiectasias and histological evidence of neuronal degeneration, which are characteristics of human AT patients, have not seen in these mice, suggesting that the mouse model for AT is limited. Thus, the established human AT-iPS cells described in this study show promise as a tool for clarifying the pathogenesis of AT, and may facilitate development of drugs that inhibit ataxia and hypersensitivity to ionizing radiation.

Methods

Ethical statement. Human cells in this study were performed in full compliance with the Ethical Guidelines for Clinical Studies (2008 Notification number 415 of the Ministry of Health, Labor, and Welfare). The cells were banked after approval of the Institutional Review Board at the National Institute of Biomedical Innovation (May 9, 2006).

Human cells. AT1OS cells were obtained from a ten-year-old Japanese boy (JCRB Cell Bank, Osaka, Japan). The patient history is contained in the original report[27]. The patient was referred to the hospital because of progressive cerebellar ataxia and repeated upper respiratory infection. He raised his head well at 5 months and walked alone at 14 months of age. At the age of 2 years, his parents first noticed his tottering gait. He suffered from severe suppurative tympanitis at 4 years of age, since then he was recurrently afflicted with upper respiratory infections. Before school age, he had already developed a progressive ataxic gait. At the age of 10 years, he could walk alone only a short distance. The neurological examination revealed hyporeflexia, choreoathetosis, oculomotor apraxia and cerebellar dysarthria. Telangiectasia was seen in his bulbar conjunctivae. He showed mild mental retardation (IQ, 72). X-ray computed tomography revealed the fourth ventricular enlargement, suggesting mild cerebellar atrophy. Laboratory tests disclosed a decreased serum level of IgA (17 mg/dl) and a markedly elevated level of α-fetoprotein (560 ng/ml). Serum IgE and IgM were within normal levels. His parents are first cousins.

AT1OS cells were cultured in culture dishes (100 mm, Becton Dickinson). All cultures were maintained at 37°C in a humidified atmosphere containing 95% air and 5% CO_2. When the cultures reached subconfluence, the cells were harvested with a Trypsin-EDTA solution (cat# 23315, IBL CO., Ltd, Gunma, Japan), and re-plated at a density of 5×10^5 cells in a 100-mm dish. Medium changes were carried out twice a week thereafter. MRC5-iPS cells were maintained on irradiated MEFs as previously described[28,29]. MRC5iPS#16 (Fetch), MRC5iPS#25 (Tic), and MRC5iPS#40 (Skipper) were used as controls for AT-iPS cells. MRC5 (ATCC, CCL-171), a parental cell of MRC5-iPS cells, is from lung fibroblasts of 14-week fetus (Caucasian male).

Generation of iPS cells. AT-iPS cells were generated according to the method as previously described[28]. Briefly, to produce VSV-G (vesicular stomatitis virus G glycoprotein) retroviruses, 293FT cells (Invitrogen) were plated at 2×10^6 cells per 10-cm culture dish with DMEM supplemented with 10% FBS, and incubated overnight. On the next day, the cells were co-transfected with pMXs-OCT4, SOX2, KLF4 or c-MYC, pCL-GagPol, and pHCMV-VSV-G vectors using the TransIT-293 reagent (Mirus Bio LLC, Madison WI). The virus-containing supernatants were collected 48 h after incubation. The supernatants were filtered through a 0.45 μm pore-size filter, centrifuged, and then resuspended in DMEM supplemented with 4 μg/ml polybrene (Nacalai Tesque, Kyoto, Japan). Human AT1OS cells were seeded at 1.0×10^5 cells per well of 6-well plate 24 h before infection. A 1 : 1 : 1 : 1 mixture of OCT3/4, SOX2, KLF4, and c-MYC viruses was added to AT1OS cells[28–31]. The retrovirus carrying the EGFP gene was infected to estimate infection efficiency in a separate experiment. One-half of the medium was changed every day and colonies were picked up at around day 28.

RT-PCR. Total RNA was isolated from cells using the TRIzol (Invitrogen) or the RNeasy Plus Mini Kit (Qiagen). cDNA was synthesized from 1 μg of total RNA using Superscript III reverse transcriptase (Invitrogen) with random hexamers according to the manufacturer's instructions. Template cDNA was PCR-amplified with gene-specific primer sets (Supplemental Table S1).

Quantitative RT-PCR. RNA was extracted from cells using the RNeasy Plus Mini kit (Qiagen). An aliquot of total RNA was reverse transcribed using an oligo (dT) primer. For the thermal cycle reactions, the cDNA template was amplified (ABI PRISM

7900HT Sequence Detection System) with gene-specific primer sets using the Platinum Quantitative PCR SuperMix-UDG with ROX (11743-100, Invitrogen) under the following reaction conditions: 40 cycles of PCR (95°C for 15 s and 60°C for 1 min) after an initial denaturation (95°C for 2 min). Fluorescence was monitored during every PCR cycle at the annealing step. The authenticity and size of the PCR products were confirmed using a melting curve analysis (using software provided by Applied Biosystems) and a gel analysis. mRNA levels were normalized using GAPDH as a housekeeping gene.

Western blot analysis. Western blot analysis of total cell lysate for p53 and phospho-p53(Ser15) and of nuclear fractions for ATM was performed as described[32]. The membrane filter was probed with the antibodies to p53 (Enzo Life Sci., BML-SA293), phosphor-p53 (S15) (Cell signaling, #9284), and ATM (MBL, PM026), and then incubated with HRP-conjugated antibody to rabbit IgG. The protein signals were detected by ECL detection (Amersham).

Immunocytochemical analysis. Cells were fixed with 4% paraformaldehyde in PBS for 10 min at 4°C. After washing with PBS and treatment with 0.2% trypsin in PBS (PBST) for 10 min at 4°C, cells were pre-incubated with blocking buffer (10% goat serum in PBS) for 30 min at room temperature, and then reacted with primary antibodies in blocking buffer for 12 h at 4°C. Followed by washing with 0.2% PBST, cells were incubated with secondary antibodies; anti-rabbit or anti-mouse IgG conjugated with Alexa 488 or 546 (1 : 300) (Invitrogen) in blocking buffer for 1 h at room temperature. Then, the cells were counterstained with DAPI and mounted.

Karyotypic analysis. Karyotypic analysis was contracted out at Nihon Gene Reserch Laboratories Inc. (Sendai, Japan). Metaphase spreads were prepared from cells treated with 100 ng/mL of Colcemid (Karyo Max, Gibco Co. BRL) for 6 h. The cells were fixed with methanol : glacial acetic acid (2 : 5) three times, and dropped onto glass slides (Nihon Gene Reserch Laboratories Inc.). Chromosome spreads were Giemsa banded and photographed. A minimum of 10 metaphase spreads were analyzed for each sample, and karyotyped using a chromosome imaging analyzer system (Applied Spectral Imaging, Carlsbad, CA).

Quantitative fluorescence in situ hybridization (Q-FISH). We measured telomere length by Q-FISH analysis as previously described[33–35]. The parental cells and iPS cells were subjected to telomere measurements by the telomere fluorescent intensities of the p- and q-arms of all the chromosomes in the metaphase spread individually. The telomere lengths were determined by the median telomere fluorescent unit values.

Exome sequencing. Approximately 2.0 μg of genomic DNA from each cell sample was sonicated to give a fragment size of 200 bp on a Covaris S220 instrument. After 5–6 cycles of PCR amplification, capture and library preparation were performed with Agilent SureSelect Human All Exon V4 + UTRs + lincRNA (80 Mb), followed by washing, elution, and additional 10-cycle PCR. Enriched libraries were sequenced on an Illumina HiSeq 1000 operated in 101-bp paired-end mode. Image analyses and base calling on all lanes of data were performed using CASAVA 1.8.2 with default parameters.

Read mapping and variant analysis. Reads from each sample were first trimmed by removing adapters and low quality bases at ends using Trimmomatic 0.22 and then aligned to the hs37d5 sequence (hg19 and decoy sequences) using the Burrows-Wheeler Aligner 0.6.2. Uniquely mapped reads were selected by a custom script, converted from sam to bam using SAMtools 0.1.18, and processed by Picard 1.83 to mark PCR duplicates. Genome Analysis Toolkit (GATK) 2.3–9 was then used to remove the duplicates, perform local realignment and map quality score recalibration to produce calibrated bam files for each sample. Multi-sample callings for SNVs were made by GATK. Target regions for variant detection were expanded to 93.9 Mb in total by following the manufacturer's instruction. The annotated VCF files were then filtered using GATK with a stringent filter setting and custom scripts. Variant calls which failed to pass the following filters were eliminated: QUAL < 400 || QD < 2.0 || MQ < 40.0 || FS > 60.0 || HaplotypeScore > 13.0 || GQ <= 60. When genotype is 0/1, 0/2, or 1/2, only SNVs that meet the following conditions were selected: both of the allelic depths >= 8 && difference of the allelic depths within twofold. When genotype is 0/0, 1/1, or 2/2, only SNVs that meet the following conditions were selected: difference of the allelic depths no less than 32-fold, one allelic depth is 1 and the other is no less than 16, or one allelic depth is 0 and the other is no less than 8. Annotations of altered bases were made using SnpEff 3.1 based on GRCh37.69[36]. Custom Perl scripts and C programs are available at http://github.com/glires/genomics/.

Structural mutation analysis. The structural mutation analysis by genome-wide SNP genotyping was performed using Illumina HumanCytoSNP-12 v2.1 DNA Analysis BeadChip Kit. The microarray contains approximately 300,000 SNP markers with an average call frequency of > 99%. Subsequent computational and manual analyses were performed using the Illumina KaryoStudio software. The data have been submitted to the GEO database under accession number GSE54576.

Irradiation. Cells were irradiated by X-ray at 0.87 Gy/min, using MBR-1520R-3 (Hitachi, Tokyo, Japan). Immediately after irradiation, cells were returned to the incubator at 37°C in a humidified atmosphere containing 95% air and 5% CO_2, and incubated until further processing. Cell number was counted with Vi-CELL 1.00. (Beckman Coulter K.K.,Tokyo, Japan).

Teratoma formation. AT-iPS cells were harvested by accutase treatment, collected into tubes, and centrifuged. The same volume of Basement Membrane Matrix (354234, BD Biosciences) was added to the cell suspension. The cells (>1×10^7) were subcutaneously inoculated into immuno-deficient, non-obese diabetic (NOD)/severe combined immunodeficiency (SCID) mice (CREA, Tokyo, Japan). After 6 to 10 weeks, the resulting tumors were dissected and fixed with PBS containing 4% paraformaldehyde. Paraffin-embedded tissue was sliced and stained with hematoxylin and eosin (HE). The operation protocols were accepted by the Laboratory Animal Care and the Use Committee of the National Research Institute for Child and Health Development, Tokyo.

Neural differentiation of iPS cells. We employed the standard protocol for neural differentiation of iPS cells[37,38]. Apoptosis was detected by the ApopTag ISOL Dual Fluorescence Apoptosis Detection Kit (DNase Types I & II) APT1000 (Millipore), according to the manufacturer's protocol.

1. Takahashi, K. & Yamanaka, S. Induction of pluripotent stem cells from mouse embryonic and adult fibroblast cultures by defined factors. *Cell* **126**, 663–676 (2006).
2. Yu, J. *et al.* Induced pluripotent stem cell lines derived from human somatic cells. *Science* **318**, 1917–1920 (2007).
3. Hankowski, K. E., Hamazaki, T., Umezawa, A. & Terada, N. Induced pluripotent stem cells as a next-generation biomedical interface. *Lab Invest* **91**, 972–977 (2011).
4. Mavrou, A., Tsangaris, G. T., Roma, E. & Kolialexi, A. The ATM gene and ataxia telangiectasia. *Anticancer Res* **28**, 401–405 (2008).
5. McKinnon, P. J. ATM and ataxia telangiectasia. *EMBO reports* **5**, 772–776 (2004).
6. Kurz, E. U. & Lees-Miller, S. P. DNA damage-induced activation of ATM and ATM-dependent signaling pathways. *DNA Repair (Amst)* **3**, 889–900 (2004).
7. Gatei, M. *et al.* Role for ATM in DNA damage-induced phosphorylation of BRCA1. *Cancer Res* **60**, 3299–3304 (2000).
8. Barlow, C. *et al.* Atm-deficient mice: a paradigm of ataxia telangiectasia. *Cell* **86**, 159–171 (1996).
9. Kinoshita, T. *et al.* Ataxia-telangiectasia mutated (ATM) deficiency decreases reprogramming efficiency and leads to genomic instability in iPS cells. *Biochem Biophys Res Commun* **407**, 321–326 (2011).
10. Kuljis, R. O., Xu, Y., Aguila, M. C. & Baltimore, D. Degeneration of neurons, synapses, and neuropil and glial activation in a murine Atm knockout model of ataxia-telangiectasia. *Proc Natl Acad Sci U S A* **94**, 12688–12693 (1997).
11. Song, H., Chung, S. K. & Xu, Y. Modeling disease in human ESCs using an efficient BAC-based homologous recombination system. *Cell Stem Cell* **6**, 80–89 (2010).
12. Lee, P. *et al.* SMRT compounds abrogate cellular phenotypes of ataxia telangiectasia in neural derivatives of patient-specific hiPSCs. *Nat Commun* **4**, 1824 (2013).
13. Nayler, S. *et al.* Induced pluripotent stem cells from ataxia-telangiectasia recapitulate the cellular phenotype. *Stem Cells Transl Med* **1**, 523–535 (2012).
14. Meek, D. W. The p53 response to DNA damage. *DNA Repair (Amst)* **3**, 1049–1056 (2004).
15. Hong, H. *et al.* Suppression of induced pluripotent stem cell generation by the p53-p21 pathway. *Nature* **460**, 1132–1135 (2009).
16. Kawamura, T. *et al.* Linking the p53 tumour suppressor pathway to somatic cell reprogramming. *Nature* **460**, 1140–1144 (2009).
17. Li, H. *et al.* The Ink4/Arf locus is a barrier for iPS cell reprogramming. *Nature* **460**, 1136–1139 (2009).
18. Marion, R. M. *et al.* A p53-mediated DNA damage response limits reprogramming to ensure iPS cell genomic integrity. *Nature* **460**, 1149–1153 (2009).
19. Utikal, J. *et al.* Immortalization eliminates a roadblock during cellular reprogramming into iPS cells. *Nature* **460**, 1145–1148 (2009).
20. Metcalfe, J. A. *et al.* Accelerated telomere shortening in ataxia telangiectasia. *Nat Genet* **13**, 350–353 (1996).
21. Marion, R. M. *et al.* Telomeres acquire embryonic stem cell characteristics in induced pluripotent stem cells. *Cell Stem Cell* **4**, 141–154 (2009).
22. Davy, P. & Allsopp, R. Balancing out the ends during iPSC nuclear reprogramming. *Cell Stem Cell* **4**, 95–96 (2009).
23. Watson, J. D. Origin of concatemeric T7 DNA. *Nat New Biol* **239**, 197–201 (1972).
24. Harley, C. B., Futcher, A. B. & Greider, C. W. Telomeres shorten during ageing of human fibroblasts. *Nature* **345**, 458–460 (1990).
25. Tchirkov, A. & Lansdorp, P. M. Role of oxidative stress in telomere shortening in cultured fibroblasts from normal individuals and patients with ataxia-telangiectasia. *Hum Mol Genet* **12**, 227–232 (2003).
26. Gore, A. *et al.* Somatic coding mutations in human induced pluripotent stem cells. *Nature* **471**, 63–67 (2011).
27. Ikenaga, M., Midorikawa, M., Abe, J. & Mimaki, T. The sensitivities to radiations and radiomimetic chemicals of cells from patients with ataxia telangiectasia. *Jinrui Idengaku Zasshi* **28**, 1–10 (1983).

28. Makino, H. *et al.* Mesenchymal to embryonic incomplete transition of human cells by chimeric OCT4/3 (POU5F1) with physiological co-activator EWS. *Exp Cell Res* **315**, 2727–2740 (2009).
29. Nishino, K. *et al.* DNA Methylation Dynamics in Human Induced Pluripotent Stem Cells over Time. *PLoS Genet* **7**, e1002085 (2011).
30. Nagata, S. *et al.* Efficient reprogramming of human and mouse primary extra-embryonic cells to pluripotent stem cells. *Genes Cells* **14**, 1395–1404 (2009).
31. Nishino, K. *et al.* Defining hypo-methylated regions of stem cell-specific promoters in human iPS cells derived from extra-embryonic amnions and lung fibroblasts. *PLoS One* **5**, e13017 (2010).
32. Toyoda, M., Kojima, M. & Takeuchi, T. Jumonji is a nuclear protein that participates in the negative regulation of cell growth. *Biochem Biophys Res Commun* **274**, 332–336 (2000).
33. Poon, S. S. & Lansdorp, P. M. Measurements of telomere length on individual chromosomes by image cytometry. *Methods Cell Biol* **64**, 69–96 (2001).
34. Terai, M. *et al.* Investigation of telomere length dynamics in induced pluripotent stem cells using quantitative fluorescence *in situ* hybridization. *Tissue Cell* **45**, 407–413 (2013).
35. Takubo, K. *et al.* Chromosomal instability and telomere lengths of each chromosomal arm measured by Q-FISH in human fibroblast strains prior to replicative senescence. *Mech Ageing Dev* **131**, 614–624 (2010).
36. Cingolani, P. *et al.* A program for annotating and predicting the effects of single nucleotide polymorphisms, SnpEff: SNPs in the genome of Drosophila melanogaster strain w1118; iso-2; iso-3. *Fly (Austin)* **6**, 80–92 (2012).
37. Chambers, S. M. *et al.* Highly efficient neural conversion of human ES and iPS cells by dual inhibition of SMAD signaling. *Nat Biotechnol* **27**, 275–280 (2009).
38. Koch, P., Opitz, T., Steinbeck, J. A., Ladewig, J. & Brüstle, O. A rosette-type, self-renewing human ES cell-derived neural stem cell with potential for in vitro instruction and synaptic integration. *Proc Natl Acad Sci U S A* **106**, 3225–3230 (2009).

Acknowledgments

We would like to express our sincere thanks to M. Yamada for fruitful discussion and critical reading of the manuscript, to H. Abe and H. Kobayashi for providing expert technical assistance, to Dr. C. Ketcham for English editing and proofreading, and to E. Suzuki, Y. Kajiyama, Y. Suehiro, and K. Saito for secretarial work. This research was supported by grants from the Ministry of Education, Culture, Sports, Science, and Technology (MEXT) of Japan; by Ministry of Health, Labor and Welfare (MHLW) Sciences research grants; by a Research Grant on Health Science focusing on Drug Innovation from the Japan Health Science Foundation; by the program for the promotion of Fundamental Studies in Health Science of the Pharmaceuticals and Medical Devices Agency; by the Grant of National Center for Child Health and Development. We acknowledge the International High Cited Research Group (IHCRG #14-104), Deanship of Scientific Research, King Saudi University, Riyadh, Kingdom of Saudi Arabia. AU thanks King Saud University, Riyadh, Kingdom of Saudi Arabia, for the Visiting Professorship.

Author contributions

A.U. designed experiments. Y.F., M.T., K.O., K.Nakamura, K.Nakabayashi, M.Y.I. and K.T. performed experiments. Y.F., M.T., K.O., K.Nakabayashi, M.Y.I., M.N., K.Hata and K.Hanaoka analyzed data. Y.F., M.T., K.O., K.Nakabayashi, S.T., M.Y.I., M.N., K.Hata, AH, and K.Hanaoka contributed reagents, materials and analysis tools. A.M. and A.U. wrote this manuscript.

Additional information

Accession codes The SNP genotyping by SNP array data was uploaded to the ncbi web site (GSE47498: Increased X-ray sensitivity and sustained chromosomal stability in Ataxia Telangiectasia-derived induced pluripotent stem (AT-iPS) cells, GSM1151202: AT1OS cells, GSM1151203: ATiPS-262 cells at passage 17, GSM1151204: ATiPS-263 cells at passage 27, GSM1151205: ATiPS-264 cells at passage 25, GSM1151206: ATiPS-024 cells at passage 25). The exome data was uploaded to the DDBJ Sequence Read Archive (DRP001084).

Supplementary information accompanies this paper at http://www.nature.com/scientificreports

Competing financial interests: The authors declare no competing financial interests.

How to cite this article: Fukawatase, Y. *et al.* Ataxia telangiectasia derived iPS cells show preserved x-ray sensitivity and decreased chromosomal instability. *Sci. Rep.* **4**, 5421; DOI:10.1038/srep05421 (2014).

The contribution of epithelial-mesenchymal transition to renal fibrosis differs among kidney disease models

Tsutomu Inoue[1,2], Akihiro Umezawa[3], Tsuneo Takenaka[1], Hiromichi Suzuki[1,2] and Hirokazu Okada[1,2]

[1]Department of Nephrology, Faculty of Medicine, Saitama Medical University, Saitama, Japan; [2]Division of Project Research, Research Center of Genomic Medicine, Saitama Medical University, Saitama, Japan and [3]Department of Reproductive Biology, National Institute for Child Health and Development, Tokyo, Japan

The impact of the epithelial-mesenchymal transition (EMT) to the formation of renal fibrosis has been debated in several lineage-tracing studies, with conflicting findings. Such disparities may have arisen from varying experimental conditions such as different disease models, the mouse strain, and type of genetic alteration used. In order to determine the contribution of these factors to EMT, we generated four kidney disease models in several mouse strains genetically modified to express enhanced green fluorescence protein (EGFP) in cortical tubular epithelial cells under the control of the γ-glutamyl transpeptidase promoter. Using this approach, the EMT was visible and quantifiable based on a count of EGFP-positive interstitial cells in the fibrotic kidney sections of the four renal disease models found to be either EMT-prone or -resistant. The EMT-prone models consisted of unilateral ureteral obstruction and ischemic nephropathy in SJL mice. The EMT-resistant models consisted of ureteral obstruction in C57B/6 and F1 (C57B/6×SJL) mice, adriamycin nephrosis in 129 mice, and nephrotoxic serum nephritis in SJL mice. Analyses of these renal disease models suggest the emergence of EMT-derived fibroblasts arises in a disease-specific and strain-dependent manner. Thus, when considering molecular mechanisms and involvement of the EMT in renal fibrosis, it is important to take into account the experimental conditions, particularly the mouse strain and type of disease model.

Kidney International (2015) **87,** 233–238; doi:10.1038/ki.2014.235; published online 9 July 2014

KEYWORDS: interstitial fibrosis; obstructive nephropathy; renal tubular epithelial cells

Correspondence: *Hirokazu Okada, Department of Nephrology, Faculty of Medicine, Saitama Medical University, 38 Morohongo, Moroyama-machi, Iruma-gun, Saitama 350-0495, Japan.*
E-mail: hirookda@saitama-med.ac.jp

Received 15 August 2013; revised 17 May 2014; accepted 22 May 2014; published online 9 July 2014

The epithelial-mesenchymal transition (EMT) has been extensively studied in the context of embryonic development. The epithelia of mature tissues may also undergo EMT in response to stress, such as inflammation and wounding, leading to fibrogenesis.[1,2] The EMT is elicited under various conditions, including *in vitro* stimulation with transforming growth factor-β1, animal models of renal fibrosis,[3] and human obstructive nephropathy.[4] However, as the occurrence of EMT in experimental kidney disease models appears to be inconsistent, the contribution of EMT to the pathogenesis of renal fibrosis remains controversial.[5–7] We speculate that differences in experimental conditions, including the disease model, murine strain, and type of genetic modification used, may account for the discrepancies observed in the reports of EMT involvement in the setting of renal fibrosis. Here, we established an *in vivo* evaluation system for EMT, and examined differences in the contribution of EMT to renal fibrosis among several mouse models of renal disease. Strain-specific differences were also evaluated in the EMT-prone renal disease model.

RESULTS AND DISCUSSION

In a preliminary experiment, we recruited EMT-prone (MCT, mProx24, and NMuMG) and EMT-resistant (EpH4) cultured epithelial cells[8,9] and confirmed their responses to EMT-inducible stimulation with transforming growth factor-β1 and epidermal growth factor (EGF). In addition, cDNA microarray analyses were performed with RNA isolated from each cell line under conditions that promote EMT induction (GEO_ID No. GSE31359), and the top 10 upregulated EMT-specific genes were identified (Supplementary Table S1 online). Among these upregulated genes, the high-mobility group A2 (HMGA2) gene and Snail1 (both of which have been previously reported to be EMT-related transcription factors) were found to be significantly associated with the EMT in the MCT (Supplementary Figure S1 online). As is well known, the occurrence of the EMT in stimulated epithelial cells is not universal, even under controlled *in vitro* conditions. We therefore decided to assess both HMGA2 and Snail1 in the following *in vivo* experiments.

We subsequently established an *in vivo* evaluation system for the study of EMT based on a Cre recombinase/LoxP recombination system under the control of the γ-glutamyltransferase (γ-GT) promoter in which kidney cortical tubular epithelial cells are permanently labeled with enhanced green fluorescent protein (EGFP). Using this system, we created γ-GT.Cre;EGFP double-transgenic (γGT-DTg) mice, which were then used to generate unilateral ureteral obstruction (UUO), ischemia–reperfusion injury, adriamycin toxicity (ADR), and nephrotoxic serum nephritis models. With the exception of the ADR model, we used fibrosis-prone SJL/J (SJL) mice[10] for all disease models, as the establishment of a progressive ADR model requires the 129S1/svImJ (129) background, which involves another type of fibrosis-prone mice.[10–12] In the normal kidneys of γGT-DTg mice, tubular epithelial cells appear green; however, no green interstitial cells were observed (Figure 1a). On the other hand, EGFP-positive interstitial cells were detected in the kidneys of the UUO and ischemia–reperfusion injury mice (Figures 1b and d, respectively), whereas only a few positive cells were found in the ADR and nephrotoxic serum nephritis mice (Figure 1e and f, respectively), indicating that the occurrence of EMT was influenced by the type of disease model. We stained the tissues for all models using Masson's trichrome staining and anti-fibronectin antibodies. It showed that interstitial fibrosis was evidently in progress in all models, regardless of the presence of EMT (Figure 2).

To verify the accuracy of our method for distinguishing interstitial cells from tubular epithelial cells, the tubular basement membranes were stained with periodic acid–Schiff (Figure 1c). Numerous green cells were observed not only in the intratubular regions but also in the intertubular regions representing the interstitium (Figure 1c). To determine the origin and properties of the EGFP-positive interstitial cells, the kidney samples obtained from the UUO mice were stained for heat-shock protein 47, CD45, and F4/80 cellular markers (Figure 3a–f). Almost all green interstitial cells were negative for CD45. The EGFP-positive cells were negative for F4/80. Numerous EGFP-positive cells were also heat-shock protein 47-positive, indicating that the population of interstitial cells was principally non-myeloidal/non-monocytic and also consisted of collagen-producing cells. We next evaluated the mRNA expression of HMGA2 and Snail1 using quantitative reverse transcriptase-polymerase chain reaction. In the UUO model, both EMT-related transcription factors were found to be significantly upregulated compared with those observed in the other models (Supplementary Figure S2 online).

Next, in order to examine the influence of the mouse genetic background, a UUO model was generated using γGT-DTg mice of strain C57BL/6J (B6), which have been well characterized as fibrosis-resistant strains,[10,12] and the first filial generation of strains B6 and SJL (F1). No GFP-positive cells were detected in the strain B6 or F1 γGT-DTg mice, although interstitial alterations were observed (Figure 1g and h, strain F1: B6×SJL). These findings are consistent with the results of previous studies in which the EMT was detected only at extremely low levels in the UUO, ischemia–reperfusion injury, and transforming growth factor-β1 transgenic mouse models of B6 mice or mixed genetic backgrounds that included B6 mice.[5–7] Therefore, the genetic background of the mice appears to be important for determining the susceptibility of the animals to EMT, as well as to renal fibrosis. We also previously reported that the F1 offspring of 129 and B6 mice display a phenotype similar to that of B6 mice.[10] Therefore, genes governing EMT susceptibility may also function in a recessive manner.

It is important to note that interstitial fibrosis progressed in the kidneys of both the ADR and nephrotoxic serum nephritis mice, even though few EMT events were detected. Although other lineage-tracing studies of the liver[13] and lungs,[14] as well as kidneys, of transgenic mice have confirmed the contribution of EMT to the development of organ fibrosis *in vivo*, our present results indicate that the EMT is not the only route for fibroblast development in adult fibrotic tissue. Fibroblasts are derived from residential stromal cells, including fibroblasts, endothelial cells,[15] and pericytes,[5,6] as well as infiltrating bone marrow–derived fibroblasts, such as fibroblast-specific protein-1-positive myeloid cells[1,16] and fibrocytes.[17,18]

In conclusion, our findings support the notion that, at least in the mouse kidney, the EMT promotes the development of interstitial fibrosis in both a disease-specific and strain-dependent manner. Although we were unable to identify the mechanisms underlying the differences in susceptibility to EMT, the difference in the expression levels of transcription factors, such as HMGA2 and Snail1, may provide us with a valuable clue to help clarify this issue. It is therefore important to consider the experimental conditions, particularly the mouse strain and disease model, when evaluating the involvement of EMT in the pathogenesis of renal fibrosis.

MATERIALS AND METHODS

Transgenic mice

Two types of transgenic mice, γ-GT.Cre and EGFP-reporter mice, were used in this study. γ-GT.Cre mice express Cre recombinase, primarily in the cortical tubular epithelia, under the control of γ-GT promoters.[1] EGFP-reporter mice carry an EGFP transgene with a floxed-STOP cassette for the fluorescence labeling of Cre-expressing cells.

In vivo experiments

Male 5- to 6-week-old double-transgenic line [γ-GT.Cre] x [floxed-STOP.EGFP] mice were used. Manipulations to generate each mouse renal disease model were carried out as previously reported.[11,14,19,20] The UUO, ischemia–reperfusion injury, nephrotoxic serum nephritis, and ADR mice models required 7, 14, 28, and 56 days, respectively, to develop appreciable numbers of interstitial cells. All animal experiments were conducted in accordance with the NIH Guidelines for the Care and Use of Laboratory Animals and approved by the Institutional Animal Care and Use Committee of Saitama Medical University. We histologically evaluated the progression of each disease model. As a result, the corresponding

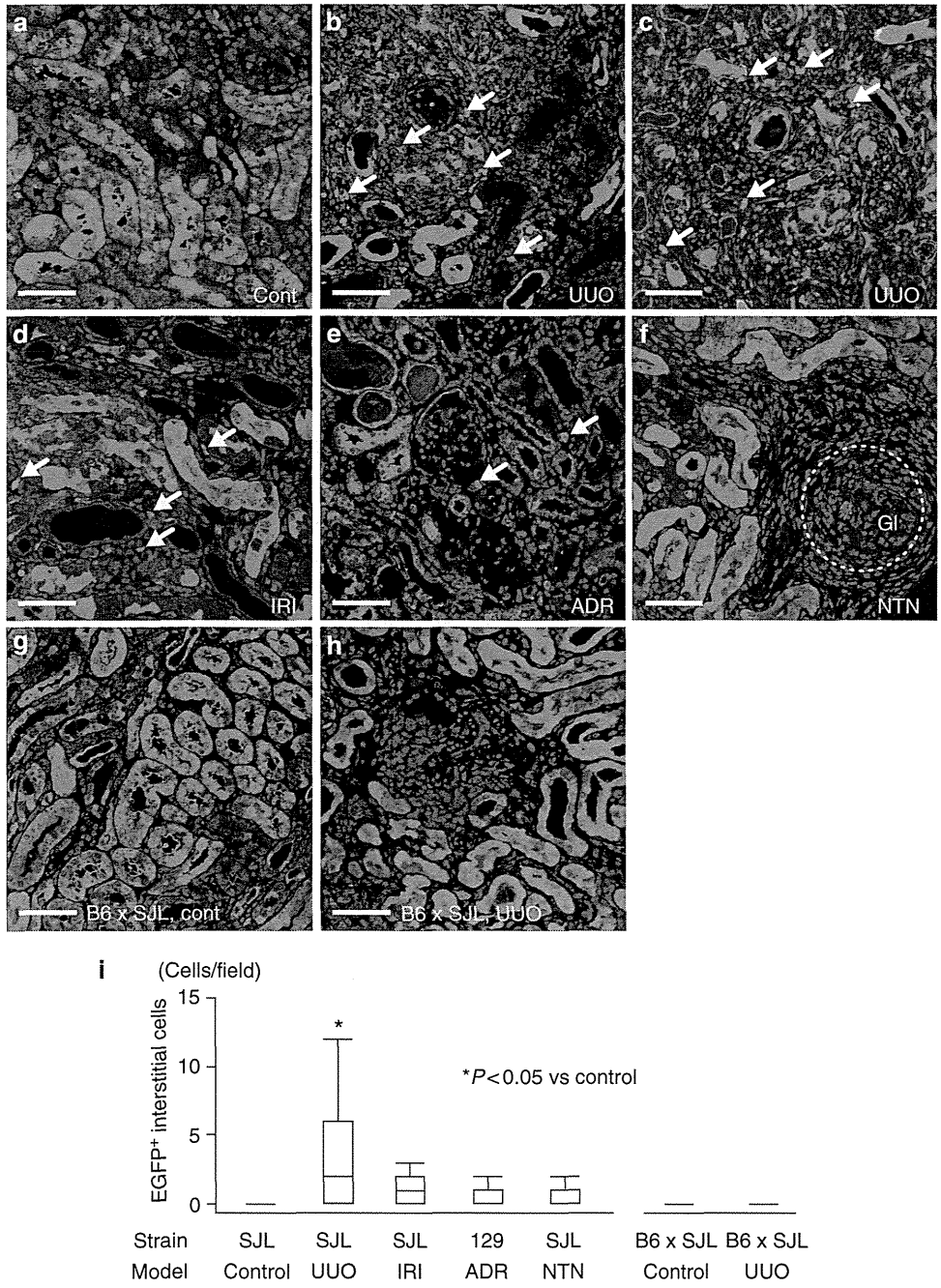

Figure 1 | Immunohistochemical analysis of the epithelial-mesenchymal transition (EMT) in the kidneys in various renal disease models established using γ-GT.Cre;EGFP double-transgenic mice. Cortical tubular epithelial cells expressing enhanced green fluorescence protein (EGFP) appear green and nuclei are stained blue. (**a**) In the control kidney, no interstitial green cells were observed. (**b**) In the kidneys of the unilateral ureteral obstruction (UUO) mice, green interstitial cells were found primarily in areas with severe tubulointerstitial alterations. (**c**) Periodic acid–Schiff (PAS) staining of the kidney sample in (**b**) showing the tubular basement membrane (red), which defines the border between the intratubular and intertubular regions (interstitium). Numerous green interstitial cells were also observed. (**d**, **e**, **f**): The ischemia–reperfusion injury (IRI) (**d**), adriamycin toxicity (ADR) (**e**), and nephrotoxic serum nephritis (NTN) (**f**) renal disease models exhibited different proportions of green interstitial cells among the total number of interstitial cells. Notably, few green interstitial cells were observed in the NTN model. (**g**, **h**) UUO model generated using γ-GT.Cre;EGFP double-transgenic mice with an F1(SJL×B6) mixed background. (**g**) In the control kidney, the majority of cortical tubular epithelial cells were stained green. (**h**) After the induction of the UUO model, few green interstitial cells were observed. (**i**) Enumeration of EGFP-expressing green interstitial cells. Significantly more green cells were detected in the kidneys of the UUO (SJL) mice than in those of the mice in the other renal disease models examined. The F1(B6×SJL) UUO mice had significantly fewer green cells than the SJL UUO model mice. The white arrows in all panels indicate EGFP-labeled interstitial cells that appeared to be derived from the tubular epithelium *via* EMT. Scale bar = 50 μm. The error bars indicate the standard deviation of five independent experiments. GI in (**f**) indicates the glomerulus.

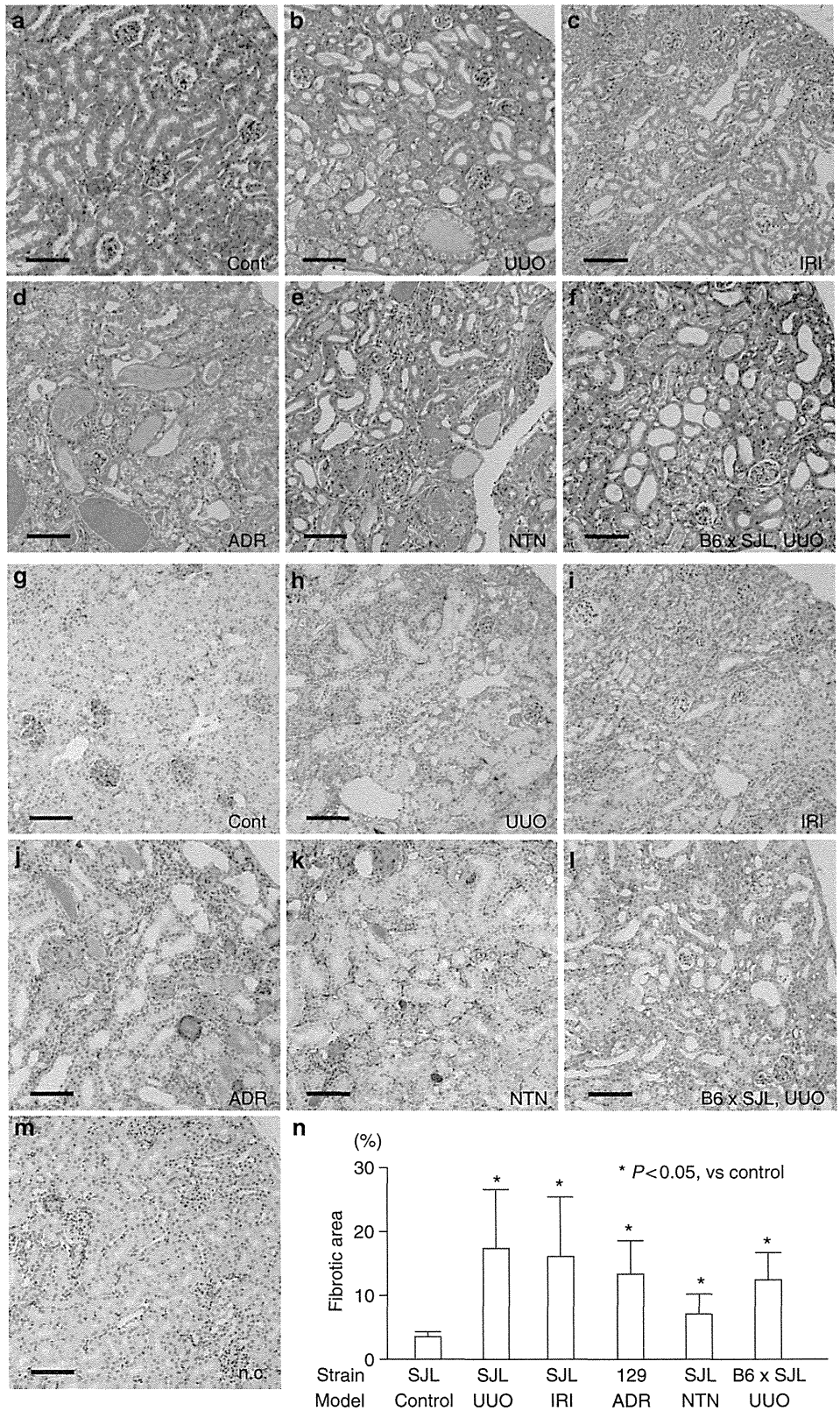

Figure 2 | Evaluation of interstitial fibrosis using Masson's trichrome staining and immunohistochemistry for fibronectin. Progression of collagen fiber deposition was observed in all disease models, regardless of the epithelial-mesenchymal transition (EMT)-prone or EMT-resistant status (**b**–**f**). In addition, fibronectin accumulation was noted in all models (**h**–**l**). Panels **a** and **g** are normal kidneys in SJL mice. Panel **m** indicates the findings of the negative control for immunohistochemistry using normal rabbit sera instead of anti-fibronectin antibodies. The results for the blue area of Masson's trichrome staining are shown in panel **n**. Scale bar = 200 μm (**a**–**m**). n.c. indicates negative control. The error bars indicate the standard deviation of five independent fields in each kidney obtained from the disease model and control groups (**n**).

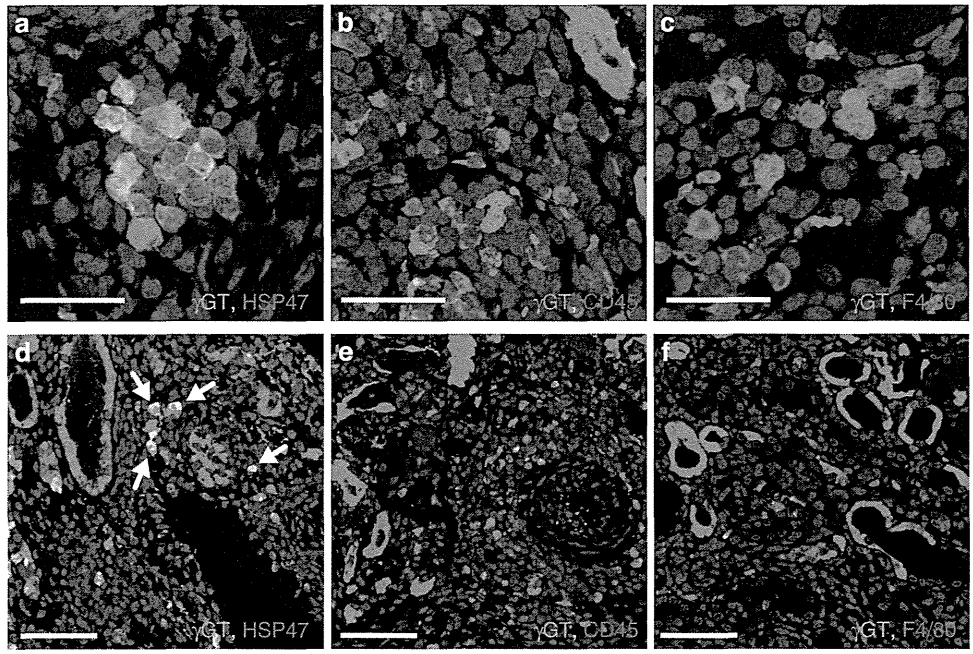

Figure 3 | Immunohistochemical characteristics of the epithelial-mesenchymal transition (EMT)-derived interstitial cells. (**a**–**f**) Immunostaining for HSP47 (**a**, **d**), CD45 (**b**, **e**), and F4/80 (**c**, **f**) in the kidneys of the unilateral ureteral obstruction (UUO) (SJL.γ-GT.Cre;EGFP double-transgenic) mice. A subpopulation of green interstitial cells expressed HSP47 (white arrows in **d**), a marker of collagen production. Scale bar = 25 μm in (**a**–**c**), 50 μm in (**d**–**f**).

functional data (proteinuria, serum creatinine, and so on) were not measured.

Immunohistochemistry

Formalin-fixed and paraffin-embedded kidney sections were prepared using standard procedures. With the exception of EGFP, a TSA kit (Molecular Probes/Invitrogen, Carlsbad, CA) was used to label primary antibodies with Alexa Fluor 555 (Molecular Probes). TO-PRO-3 (Molecular Probes) was used to detect nuclei. EGFP was detected using an anti-EGFP antibody followed by an Alexa Fluor 555–labeled secondary antibody.

The complete Materials and Methods are available online as Supplementary material.

DISCLOSURE

All the authors declared no competing interests.

ACKNOWLEDGMENTS

This work was supported in part by research grants from the Japanese Ministry of Education, Culture, Sports, Science and Technology and Asubio Pharma.

SUPPLEMENTARY MATERIAL

Table S1. Top 10 genes upregulated in the EMT-prone cultured cell lines only after co-stimulation with transforming growth factor-β1 and EGF for 24 hours.

Figure S1. Involvement of the EMT transcriptional regulators, Snail1 and HMGA2, in the EpH4 and MCT cells.

Figure S2. Quantitative analysis of the EMT-related-factors, Snail1 and HMGA2, using qRT-PCR.

Supplementary material is linked to the online version of the paper at http://www.nature.com/ki

REFERENCES

1. Iwano M, Plieth D, Danoff TM *et al.* Evidence that fibroblasts derive from epithelium during tissue fibrosis. *J Clin Invest* 2002; **110**: 341–350.
2. Zeisberg M, Neilson EG. Biomarkers for epithelial-mesenchymal transitions. *J Clin Invest* 2009; **119**: 1429–1437.
3. Quaggin SE, Kapus A. Scar wars: mapping the fate of epithelial-mesenchymal-myofibroblast transition. *Kidney Int* 2011; **80**: 41–50.
4. Inoue T, Okada H, Takenaka T *et al.* A case report suggesting the occurrence of epithelial-mesenchymal transition in obstructive nephropathy. *Clin Exp Nephrol* 2009; **13**: 385–388.
5. Humphreys BD, Lin SL, Kobayashi A *et al.* Fate tracing reveals the pericyte and not epithelial origin of myofibroblasts in kidney fibrosis. *Am J Pathol* 2010; **176**: 85–97.
6. Koesters R, Kaissling B, Lehir M *et al.* Tubular overexpression of transforming growth factor-beta1 induces autophagy and fibrosis but not mesenchymal transition of renal epithelial cells. *Am J Pathol* 2010; **177**: 632–643.
7. Lin SL, Kisseleva T, Brenner DA *et al.* Pericytes and perivascular fibroblasts are the primary source of collagen-producing cells in obstructive fibrosis of the kidney. *Am J Pathol* 2008; **173**: 1617–1627.
8. Brown KA, Aakre ME, Gorska AE *et al.* Induction by transforming growth factor-beta1 of epithelial to mesenchymal transition is a rare event *in vitro*. *Breast Cancer Res* 2004; **6**: R215–R231.
9. Inoue T, Okada H, Kobayashi T *et al.* Hepatocyte growth factor counteracts transforming growth factor-beta1, through attenuation of connective tissue growth factor induction, and prevents renal fibrogenesis in 5/6 nephrectomized mice. *FASEB J* 2003; **17**: 268–270.
10. Kato N, Watanabe Y, Ohno Y *et al.* Mapping quantitative trait loci for proteinuria-induced renal collagen deposition. *Kidney Int* 2008; **73**: 1017–1023.
11. Artunc F, Nasir O, Amann K *et al.* Serum- and glucocorticoid-inducible kinase 1 in doxorubicin-induced nephrotic syndrome. *Am J Physiol Renal Physiol* 2008; **295**: F1624–F1634.
12. Ma LJ, Fogo AB. Model of robust induction of glomerulosclerosis in mice: importance of genetic background. *Kidney Int* 2003; **64**: 350–355.
13. Zeisberg M, Yang C, Martino M *et al.* Fibroblasts derive from hepatocytes in liver fibrosis via epithelial to mesenchymal transition. *J Biol Chem* 2007; **282**: 23337–23347.

14. Kim J, Seok YM, Jung KJ *et al.* Reactive oxygen species/oxidative stress contributes to progression of kidney fibrosis following transient ischemic injury in mice. *Am J Physiol Renal Physiol* 2009; **297**: F461–F470.
15. Zeisberg EM, Tarnavski O, Zeisberg M *et al.* Endothelial-to-mesenchymal transition contributes to cardiac fibrosis. *Nat Med* 2007; **13**: 952–961.
16. Inoue T, Plieth D, Venkov CD *et al.* Antibodies against macrophages that overlap in specificity with fibroblasts. *Kidney Int* 2005; **67**: 2488–2493.
17. Bucala R, Spiegel LA, Chesney J *et al.* Circulating fibrocytes define a new leukocyte subpopulation that mediates tissue repair. *Mol Med* 1994; **1**: 71–81.
18. Sakai N, Wada T, Yokoyama H *et al.* Secondary lymphoid tissue chemokine (SLC/CCL21)/CCR7 signaling regulates fibrocytes in renal fibrosis. *Proc Natl Acad Sci USA* 2006; **103**: 14098–14103.
19. Okada H, Inoue T, Kikuta T *et al.* Poly(ADP-ribose) polymerase-1 enhances transcription of the profibrotic CCN2 gene. *J Am Soc Nephrol* 2008; **19**: 933–942.
20. Okada H, Inoue T, Kikuta T *et al.* A possible anti-inflammatory role of angiotensin II type 2 receptor in immune-mediated glomerulonephritis during type 1 receptor blockade. *Am J Pathol* 2006; **169**: 1577–1589.

ARTICLE
PUBLISHED ONLINE: 22 JUNE 2014 | DOI: 10.1038/NCHEMBIO.1552
nature chemical biology

Notch inhibition allows oncogene-independent generation of iPS cells

Justin K Ichida[1,2,9,10], Julia TCW[1-3,10], Luis A Williams[1,2], Ava C Carter[1,2], Yingxiao Shi[9], Marcelo T Moura[1,2], Michael Ziller[1,4], Sean Singh[1,2], Giovanni Amabile[5], Christoph Bock[1,4], Akihiro Umezawa[6], Lee L Rubin[1], James E Bradner[7,8], Hidenori Akutsu[6]*, Alexander Meissner[1,4]* & Kevin Eggan[1-3]*

The reprogramming of somatic cells to pluripotency using defined transcription factors holds great promise for biomedicine. However, human reprogramming remains inefficient and relies either on the use of the potentially dangerous oncogenes *KLF4* and *CMYC* or the genetic inhibition of the tumor suppressor gene *p53*. We hypothesized that inhibition of signal transduction pathways that promote differentiation of the target somatic cells during development might relieve the requirement for non-core pluripotency factors during induced pluripotent stem cell (iPSC) reprogramming. Here, we show that inhibition of Notch greatly improves the efficiency of iPSC generation from mouse and human keratinocytes by suppressing p21 in a p53-independent manner and thereby enriching for undifferentiated cells capable of long-term self-renewal. Pharmacological inhibition of Notch enabled routine production of human iPSCs without KLF4 and CMYC while leaving p53 activity intact. Thus, restricting the development of somatic cells by altering intercellular communication enables the production of safer human iPSCs.

Use of the potent oncogenes *KLF4* and *MYC* (henceforth referred to as *CMYC*) in the generation of iPSCs limits their translational utility[1,2]. Currently, elimination of these genes during human iPSC reprogramming requires suppression of p53 activity[2–16], which in turn results in the accumulation of genetic mutations in the resulting iPSCs[8]. Therefore, there remains a real need for reprogramming approaches that enable iPSC generation without the use of *KLF4* and *CMYC* while leaving p53 activity intact.

In part to address this need, several groups have undertaken chemical screens to identify small molecules that can improve reprogramming[17–21]. Thus far, the majority of active compounds are thought to improve reprogramming by inhibiting chromatin-modifying enzymes or by reinforcing the transcriptional network associated with the pluripotent state[17–22]. Consistent with their proposed mechanisms of action, these chemicals generally function in cellular intermediates that arise late in reprogramming, catalyzing their final conversion into iPSCs[19,22]. It is currently unclear whether known chemicals are sufficient for generating iPSCs from adult human cells, which are consistently more difficult to reprogram than mouse embryonic fibroblasts[23].

Given the likely need for additional reprogramming chemicals and the knowledge that most known compounds act late in this process, we reasoned that it would be valuable to identify small molecules that improve reprogramming by acting early, perhaps within the somatic cells themselves. We reasoned that one approach toward this goal would be to identify chemicals that could modulate signal transduction cascades in somatic cell populations to enrich for those cells with an enhanced capacity for reprogramming. We reasoned that if such compounds could be identified, they might expand the translational utility of chemical reprogramming.

It has been recognized that the extent of a target cell's differentiation is an important determinant of the efficiency by which it can be reprogrammed[24–26]. We therefore hypothesized that chemically driving somatic cells into a more potent 'stem cell' state might improve their reprogramming. To test this hypothesis, we chose to ask whether known chemical inhibitors of the Notch signaling pathway could aid in reprogramming.

The Notch signaling pathway is highly conserved and regulates the proliferation and differentiation of many distinct progenitor cell and stem cell types[27]. Notch ligands are generally transmembrane proteins that require contact between two cells to mediate signal transduction[28]. In skin, Notch promotes differentiation by directly activating *CDKN1A* (henceforth referred to as *p21*) expression, which in turn blocks proliferation and induces the differentiation of keratinocyte stem cell populations[29,30]. We therefore hypothesized that inhibition of Notch in keratinocytes might enhance iPSC generation by inhibiting differentiation and enriching more easily reprogrammed progenitor cells. We also felt that keratinocytes were an attractive model for testing our hypothesis because if Notch inhibition did have an effect, it could be immediately translated to the production of patient-specific iPSCs[31,32].

Here, we show that Notch inhibition improves the efficiency of iPSC generation from mouse and human keratinocytes by suppressing p21 and thereby enriching undifferentiated cells with increased reprogramming potential. In addition, pharmacological inhibition of Notch enabled the efficient production of human iPSCs without *KLF4* and *CMYC* while leaving p53 activity intact, resulting in the production of safer human iPSCs.

[1]Harvard Stem Cell Institute, Department of Stem Cell and Regenerative Biology, Harvard University, Cambridge, Massachusetts, USA. [2]Howard Hughes Medical Institute, Stanley Center for Psychiatric Research, Cambridge, Massachusetts, USA. [3]Department of Molecular and Cellular Biology, Harvard University, Cambridge, Massachusetts, USA. [4]Broad Institute of MIT and Harvard, Cambridge, Massachusetts, USA. [5]Harvard Stem Cell Institute, Harvard Medical School, Boston, Massachusetts, USA. [6]Department of Reproductive Biology, National Research Institute for Child Health and Development, Tokyo, Japan. [7]Department of Medical Oncology, Dana-Farber Cancer Institute, Boston, Massachusetts, USA. [8]Department of Medicine, Harvard Medical School, Boston, Massachusetts, USA. [9]Department of Stem Cell Biology and Regenerative Medicine, University of Southern California, Los Angeles, California, USA. [10]These authors contributed equally to this work. *e-mail: akutsu-h@ncchd.go.go.jp, alexander_meissner@harvard.edu or keggan@scrb.harvard.edu

RESULTS

DAPT treatment promotes keratinocyte reprogramming

Notch signaling is activated by the γ-secretase complex, which cleaves the membrane-tethered Notch receptor upon ligand binding and generates a free intracellular domain that can translocate to the nucleus and modulate transcription[27]. It has previously been shown that the γ-secretase inhibitor DAPT (**Fig. 1a**) can block Notch signaling in mouse keratinocytes[33]. As expected, 10 μM DAPT treatment of both neonatal mouse and human keratinocytes transduced with the iPSC reprogramming factors increased the abundance of the full-length Notch receptor, reduced levels of cleaved Notch intracellular domain (**Supplementary Results**, **Supplementary Fig. 1a**) and decreased expression of the Notch-target genes *Hey1*, *Hes1*, *Hes5* and *Col6a1* (**Supplementary Fig. 1b**).

To determine whether inhibition of Notch could increase the efficiency of reprogramming, we used *Pou5f1* (henceforth referred to as *Oct4*), *Sox2*, *Klf4* and *cMyc* to transduce *Oct4*::GFP mouse or human keratinocytes and cultured the resulting cells for 25 d either in the presence or absence of DAPT. We found that the addition of 10 μM DAPT led to a fourfold increase in the number of resulting *Oct4*::GFP+ mouse and NANOG+/TRA-1-81+ human iPSC colonies (**Fig. 1b**).

We wondered whether this increase in reprogramming activity might allow the generation of iPSCs from keratinocytes without *Klf4* and *cMyc*. Indeed, although transduction of *Oct4* and *Sox2* alone were not sufficient to induce keratinocyte reprogramming, *Oct4* and *Sox2* combined with DAPT treatment routinely yielded mouse and human iPSC colonies (**Fig. 1c,d** and **Supplementary Fig. 2a**). This effect was specific to *Oct4*- and *Sox2*-transduced cells because other two-factor combinations did not yield iPSCs in the presence of DAPT (**Fig. 1c**).

To determine whether these putative iPS cell lines were pluripotent, we subjected them to a 'scorecard' assay for pluripotency that we recently developed[34]. We found that these cell lines were indeed composed of pluripotent cells and that they performed comparably to human embryonic stem cells in their expression of pluripotency-associated genes and differentiation propensities (**Supplementary Fig. 2b,c**). To further confirm their differentiation capacity, we also injected the *OCT4*, *SOX2*+ DAPT human cells into immunocompromised mice and found that they readily formed teratomas containing differentiated cells (**Fig. 1e**). Moreover, when injected into blastocysts, the *Oct4*, *Sox2*+ DAPT mouse cells contributed to the germline, producing chimeric mice (**Supplementary Fig. 2d,e**).

Many applications of iPSCs would require the DAPT-dependent generation of *KLF4*- and *CMYC*-free iPSCs from adult keratinocytes. Therefore, we determined whether DAPT treatment increased the reprogramming potential of adult human keratinocytes. As with mouse and human neonatal keratinocytes, we found that DAPT treatment of *KLF4*-, *SOX2*-, *OCT4*- and *CMYC*-transduced adult human keratinocytes markedly improved their rate of reprogramming (**Supplementary Fig. 2f**) and also enabled the generation of iPSCs with just *OCT4* and *SOX2* (**Fig. 1f** and **Supplementary Fig. 2g**). The scorecard assay again verified that these two-factor iPSCs were pluripotent (**Supplementary Fig. 2b,c**). Together, these results demonstrate that DAPT reliably enables the generation of bona fide mouse and human iPSCs from keratinocytes without *KLF4* and *CMYC*.

Notch inhibition promotes reprogramming

Our results thus far suggest that antagonizing Notch signaling in keratinocytes may promote their conversion into iPSCs. To begin verifying that NOTCH was indeed the functional target of DAPT during reprogramming, we tested a structurally distinct γ-secretase inhibitor, DBZ[35] (**Fig. 2a**), for activity in iPSC generation. When we treated human keratinocytes with DBZ, we observed

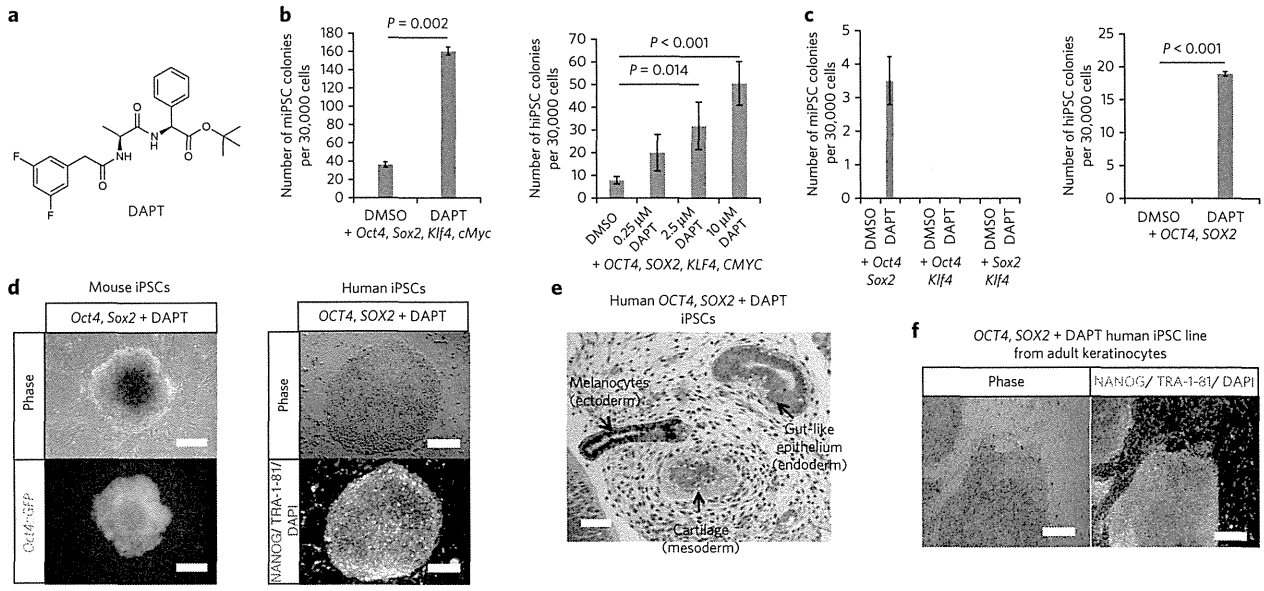

Figure 1 | DAPT treatment promotes mouse and human keratinocyte reprogramming. (**a**) Chemical structure of DAPT. (**b**) The efficiency of iPSC generation from mouse (left) and human (right) keratinocytes transduced with *Oct4*, *Sox2*, *Klf4* and *cMyc* with DMSO or DAPT treatment (DAPT used at 10 μM in mouse experiment). (**c**) The efficiency of iPSC generation from mouse (left) and human (right) keratinocytes transduced with all combinations of two reprogramming factors with DMSO or 2.5 μM DAPT treatment from days 1–18 after transduction. (**d**) A P0 mouse and human iPSC colony generated using *OCT4*, *SOX2* and DAPT. Scale bars, 100 μm. (**e**) Teratoma generated by iPSCs derived from human neonatal kerationcytes using *OCT4*, *SOX2* and DAPT. Scale bar, 50 μm. (**f**) NANOG+/TRA-1-81+ iPSC line generated from human adult keratinocytes using *OCT4*, *SOX2*+ DAPT. Scale bars, 100 μm. For all experiments, error bars represent the s.d. between two or three biological replicates, and statistical significance was determined using a two-tailed homoscedastic Student's *t*-test.

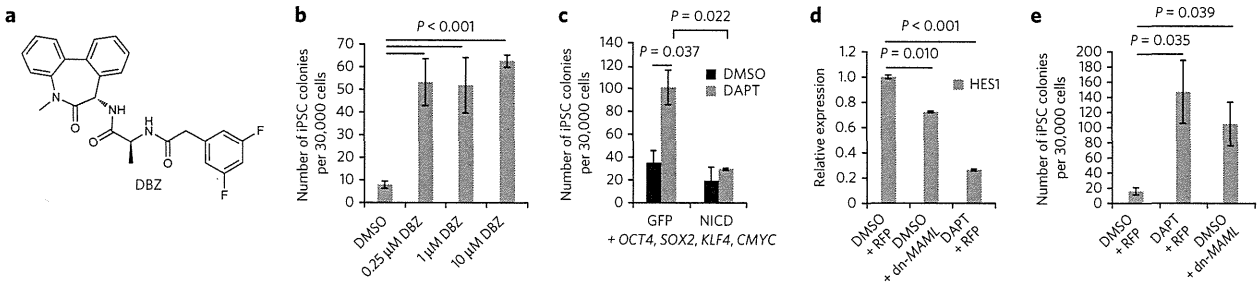

Figure 2 | γ-secretase inhibition promotes reprogramming by blocking Notch signaling. (**a**) Chemical structure of DBZ. (**b**) The efficiency of NANOG+/TRA-1-81+ iPSC generation from human neonatal keratinocytes transduced with *OCT4*, *KLF4*, *SOX2* and *CMYC* and treated with different concentrations of DBZ from days 1-18 after transduction. (**c**) The efficiency of NANOG+/ TRA-1-81+ iPSC generation from human neonatal keratinocytes transduced with *OCT*, *SOX2*, *KLF4* and *CMYC* and GFP or NOTCH intracellular domain (NICD) and treated with DMSO or 10 μM DAPT from days 1-18 after transduction. Cells were transduced with NOTCH ICD or GFP lentivirus 1 day after transduction with the reprogramming factors. (**d**) qPCR analysis of expression levels of NOTCH-dependent gene HES1 in human neonatal keratinocytes transduced with dominant-negative MASTERMIND-LIKE-1 (dn-*MAML1*) or RFP. (**e**) The efficiency of NANOG+/TRA-1-81+ iPSC generation from human neonatal keratinocytes transduced with *OCT*, *SOX2*, *KLF4* and *CMYC* and RFP or dn-*MAML1* and treated with DMSO or 10 μM DAPT from days 1-18 after transduction. For all experiments, error bars represent the s.d. between two or three biological replicates, and statistical significance was determined using a two-tailed homoscedastic Student's *t*-test.

reductions in the levels of the intracellular domain of the NOTCH receptor (**Supplementary Fig. 1a**) and the NOTCH-dependent genes *HES1* and *HES5* (**Supplementary Fig. 3a**), indicating that DBZ administration inhibited NOTCH signaling. Consistent with the notion that NOTCH inhibition increases the rate of reprogramming, DBZ stimulated the formation of human iPSC colonies (**Fig. 2b**).

Both DBZ and DAPT could have effects on the processing of unidentified γ-secretase substrates that are distinct from NOTCH, which might also affect reprogramming efficiency. If the beneficial effects of DAPT on reprogramming were being mediated through the specific inhibition of NOTCH signaling rather than through some other target of γ-secretase, then we reasoned that constitutive activation of NOTCH signaling should eliminate the beneficial effect

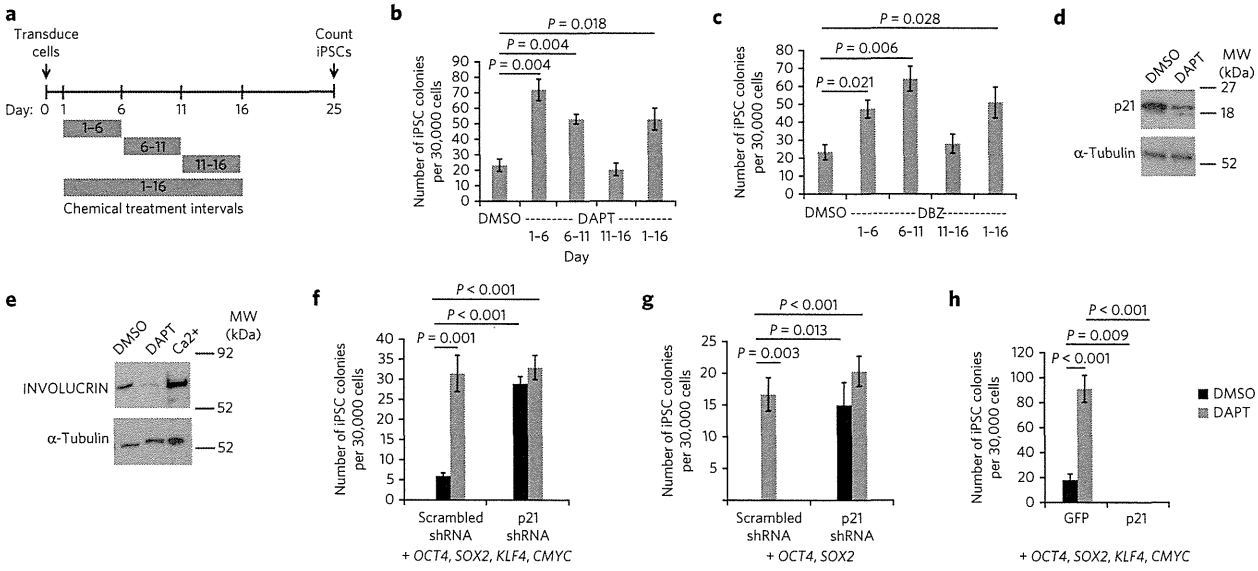

Figure 3 | Notch inhibition promotes keratinocyte reprogramming by suppressing p21. (**a**) Schematic of the DAPT treatment time course on human neonatal keratinocytes. (**b**,**c**) Efficiency of NANOG+/TRA-1-81+ iPSC generation from human neonatal keratinocytes transduced with *OCT4*, *SOX2*, *KLF4* and *CMYC* and treated with intervals of 10 μM DAPT (**b**) or 2 μM DBZ (**c**). (**d**) Western blot for p21 in human neonatal keratinocytes transduced with *OCT4* and *SOX2* and treated with DMSO or 10 μM DAPT. The full blot is shown in **Supplementary Figure 7c**. (**e**) Western blot for INVOLUCRIN in human neonatal keratinocytes treated with DMSO, 10 μM DAPT or 1.2 mM calcium chloride for 6 d. Calcium was used as a positive control to induce keratinocyte differentiation. The full blot is shown in **Supplementary Figure 7d**. (**f**) Efficiency of NANOG+/TRA-1-81+ iPSC generation from human neonatal keratinocytes transduced with *OCT4*, *KLF4*, *SOX2* and *CMYC* and a scrambled shRNA or a p21 shRNA at day 0 of reprogramming. DAPT was added at 10 μM. (**g**) Efficiency of NANOG+/TRA-1-81+ iPSC generation from human neonatal keratinocytes transduced with *OCT4* and *SOX2* and a scrambled shRNA control or a p21 shRNA at day 0 of reprogramming. DAPT was added at 2.5 μM. (**h**) Efficiency of NANOG+/TRA-1-81+ iPSC generation from human neonatal keratinocytes transduced with *OCT*, *SOX2*, *KLF4* and *CMYC* and GFP or p21 and treated with DMSO or 10 μM DAPT from days 1-18 after transduction. For all experiments, error bars represent the s.d. between two or three biological replicates, and statistical significance was determined using a two-tailed homoscedastic Student's *t*-test.

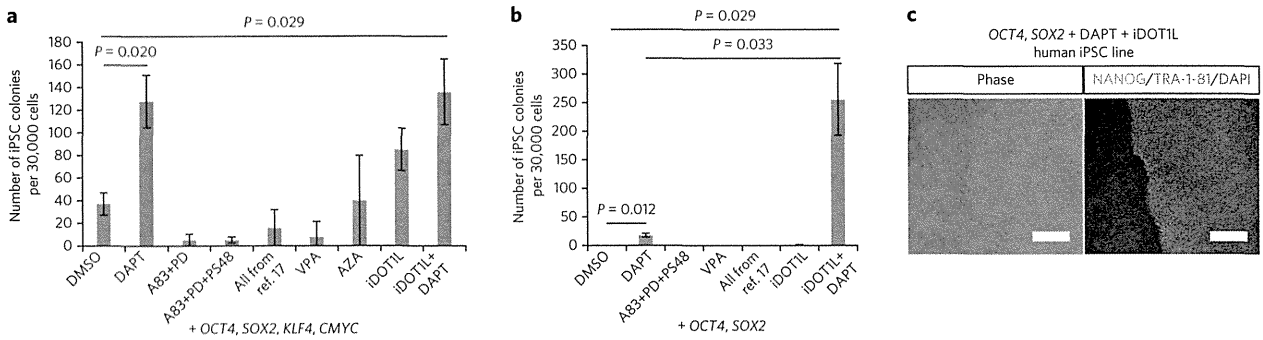

Figure 4 | Highly efficient reprogramming with NOTCH and DOT1L inhibition. (**a**) Comparison of NANOG+/TRA-1-81+ iPSC generation from *OCT4*, *SOX2*, *KLF4* and *CMYC*-transduced human neonatal keratinocytes using 10 μM DAPT versus other published reprogramming chemicals. A83, A8301 (0.5 μM); PD, PD0325901 (0.5 μM); 'All from ref. 17', A8301 (0.5 μM), PD0325901 (0.5 μM), PS48 (5 μM), sodium butyrate (0.25 mM), Parnate (2 μM) and CHIR99021 (3 μM); AZA, 5-aza-cytidine (0.5 μM); VPA, valproic acid (0.5 mM); iDOT1L, EPZ004777 (3 μM). (**b**) Comparison of NANOG+/TRA-1-81+ iPSC generation from *OCT4*- and *SOX2*- transduced human neonatal keratinocytes using 2.5 μM DAPT versus other published reprogramming chemicals. (**c**) iPSC line generated from human neonatal keratinocytes using *OCT4*, *SOX2*, DAPT and iDOT1L. Scale bars, 100 μm. For all experiments, error bars represent the s.d. between two or three biological replicates, and statistical significance was determined using a two-tailed homoscedastic Student's *t*-test.

of DAPT. Consistent with this notion, we found that overexpression of the NOTCH intracellular domain (**Supplementary Fig. 3b**) stimulated the expression of NOTCH-target genes (**Supplementary Fig. 3c**) and completely blocked the positive effects of DAPT on reprogramming (**Fig. 2c**). Conversely, we reasoned that antagonizing the transcriptional activity of NOTCH should increase the rate of keratinocyte reprogramming. Indeed, when we suppressed NOTCH activity by overexpressing a dominant-negative form of *MAML1* (**Fig. 2d**), a transcriptional co-activator for NOTCH[36,37], we observed an increase in iPSC generation from keratinocytes transduced with all four reprogramming factors (**Fig. 2e**). Therefore, we conclude that the inhibition of NOTCH signaling promotes the reprogramming of both human and mouse keratinocytes.

To understand how Notch inhibition promotes iPSC generation, we first determined when in the reprogramming process it was required. We treated mouse keratinocytes with DAPT either before or both before and after transduction with reprogramming factors. Although treatment both before and after transduction yielded a fourfold increase in iPSC generation, we found that pretreatment alone resulted in a 2.5-fold enhancement in reprogramming efficiency (**Supplementary Fig. 4a**). To more precisely pinpoint the effective post-transduction treatment window, we transduced human keratinocytes with *KLF4*, *OCT4*, *SOX2* and *CMYC* and administered DAPT or DBZ from days 1–6, 6–11, 11–16 or 1–16 after viral infection (**Fig. 3a–c**). Chemical inhibition of NOTCH signaling was most effective during early time points, increasing iPSC generation when used from days 1–6 and 6–11 (**Fig. 3b,c**). In contrast, a later treatment from days 11–16 had little effect on reprogramming (**Fig. 3b,c**). Together, these results indicate that Notch inhibition can act on the starting keratinocytes and at early time points just after the initiation of transcription factor overexpression to enhance reprogramming.

Notch inhibition acts by suppressing p21 expression

One way that Notch inhibition could promote iPSC formation is by activating the expression of the reprogramming transcription factors from their endogenous loci. However, when we treated human keratinocytes with DAPT and analyzed their gene expression, we found that levels of *KLF4*, *OCT4* and *CMYC* actually decreased, and *SOX2* levels did not change (**Supplementary Fig. 4b**).

In the mammalian epidermis, Notch signaling functions as a switch that directly activates *p21* transcription, which in turn forces keratinocytes to exit the cell cycle and begin differentiating[38]. To determine whether chemical inhibition of Notch signaling in keratinocytes might be enhancing their reprogramming potential by suppressing *p21*, we measured p21 levels in human keratinocytes in the presence and absence of DAPT. Consistent with previous reports[38], we found that Notch inhibition decreased the levels of *p21* mRNA and protein in these cells (**Fig. 3d** and **Supplementary Fig. 4c**). In addition, DAPT treatment slightly decreased the level of Flag-tagged p21 protein expressed by an exogenous retrovirus, indicating that Notch may also regulate p21 after transcription (**Supplementary Fig. 4d,e**). Consistent with these observations, Notch inhibition suppressed expression of INVOLUCRIN, which is expressed in more differentiated keratinocytes (**Fig. 3e**).

To verify that Notch inhibition promotes iPSC reprogramming by suppressing p21, we performed two-factor (*Oct4* and *Sox2*) and four-factor reprogramming in keratinocytes with p21 siRNA and shRNA in the presence or absence of DAPT. Mouse keratinocytes transduced with *Klf4*, *Sox2*, *Oct4* and *cMyc* showed a similar increase in iPSC generation when treated with either 2.5 μm DAPT or p21 siRNA (**Supplementary Fig. 4f**). The efficiency of reprogramming with these two methods was not measurably different (**Supplementary Fig. 4f**), and treating with DAPT in the presence of the p21 siRNA did not produce a demonstrable increase in iPSC formation (**Supplementary Fig. 4f**). Similarly, suppression of p21 by shRNA (**Supplementary Fig. 4g,h**) enabled the generation of iPSCs from human keratinocytes transduced with two or four factors at rates equivalent to DAPT treatment (**Fig. 3f,g**). Again, supplementing p21 knockdown with DAPT treatment did not result in an increase in iPSC formation (**Fig. 3f,g**). These results indicate that p21 suppression and DAPT have similar effects on iPSC generation from keratinocytes and that DAPT does not provide an additional advantage over p21 suppression alone.

If Notch inhibition and p21 suppression indeed blocks keratinocyte differentiation, the p21-treated keratinocytes would be predicted to display an increase in their long-term proliferative capacity[39]. The ability to form large colonies on collagen demonstrates the ability of keratinocytes to self-renew extensively and is a functional property unique to undifferentiated cells of this lineage[39]. In contrast, differentiated keratinocytes senesce after only a few rounds of division and do not form colonies[39]. DAPT treatment of human keratinocytes for 6 d markedly increased the number of cells capable of forming large colonies when cultured for an additional 14 d in the absence of the chemical (**Supplementary Fig. 4i**). The resulting fourfold increase in colony formation rate

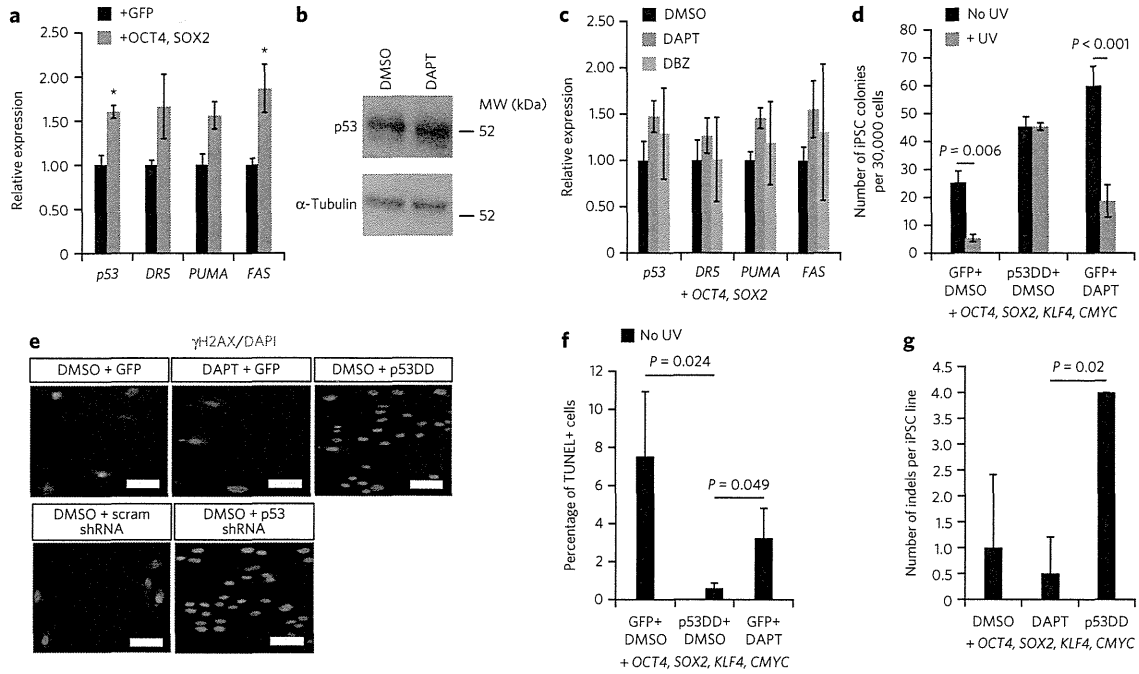

Figure 5 | NOTCH inhibition suppresses p21 without reducing p53 activity. (**a**) qPCR analysis of p53-dependent genes in human neonatal keratinocytes 3 d after transduction of GFP or *OCT4* and *SOX2*. (**b**) Western blot of p53 levels in human neonatal keratinocytes with DMSO or 10 μM DAPT treatment for 3 d. The full blot is shown in **Supplementary Figure 7g**. (**c**) qPCR analysis of p53-dependent genes after 10 μM DAPT or 2 μM DBZ treatment for 3 d in *OCT4*, *SOX2*-transduced human keratinocytes. (**d**) The efficiency of NANOG+/TRA-1-81+ iPSC generation in *OCT4*, *SOX2*, *KLF4* and *CMYC*-transduced human neonatal keratinocytes transduced with p53DD or GFP with or without exposure to UV irradiation. (**e**) γH2AX immunostaining in human neonatal keratinocytes 10 d after transduction with *OCT4*, *SOX2*, *KLF4* and *CMYC* and treatment with DAPT, p53DD or p53 shRNA. Scale bars, 50 μm. (**f**) The percentage of TUNEL-positive cells in human neonatal keratinocyte reprogramming cultures with active or inactive p53 (p53DD expression) 10 d after transduction with *OCT4*, *SOX2*, *KLF4* and *CMYC*. (**g**) The number of insertions or deletions (indels) per iPSC line derived under normal, DAPT or p53DD conditions, as determined by array comparative genomic hybridization (CGH). For all experiments, error bars represent the s.d. between two biological replicates, and statistical significance was determined using a two-tailed homoscedastic Student's *t*-test. $^*P < 0.05$.

was similar in magnitude to the elevation in iPSC generation with DAPT treatment (**Fig. 1b**). To determine whether this increased self-renewal capacity was indeed promoting reprogramming, we transduced keratinocytes with p21 to limit their replication and attempted to reprogram them either with or without DAPT. The forced p21 expression severely impaired the self-renewal potential of the keratinocytes (**Supplementary Fig. 4j**) and inhibited iPSC formation after transduction with the four reprogramming factors and treatment with DAPT (**Fig. 3h**).

Because Notch inhibition does not promote fibroblast replication[40], if this is the mechanism by which DAPT improves reprogramming, we would not expect chemical treatment to affect mouse embryonic fibroblast[41] reprogramming[41]. Indeed, DAPT treatment of MEFs transduced with all four reprogramming factors did not affect the rate of iPSC generation (**Supplementary Fig. 4k**). Together, these results demonstrate that Notch inhibition promotes iPSC generation from keratinocytes by repressing their differentiation and enhancing their long-term replicative potential through p21 suppression.

Efficient reprogramming with Notch and DOT1L inhibition

Knowing that Notch inhibition enhances iPSC generation through this unique mechanism, we next wanted to compare its activity to previously described reprogramming molecules that act through other mechanisms[17,42–44] and identify any that DAPT might synergize with. When we transduced human neonatal keratinocytes with *KLF4*, *SOX2*, *OCT4* and *CMYC* and treated them with various combinations of compounds shown to enhance reprogramming in other reports, including an activator of 3′-phosphoinositide-dependent kinase-1 (ref. 17); inhibitors of TGF-β, MEK and GSK3β signaling[17]; histone deacetylase inhibitors[17,42]; histone methyltransferase inhibitors[17,44]; and a DNA methyltransferase inhibitor[43], we found that DAPT treatment was the most potent at enhancing reprogramming (**Fig. 4a**). This remained true when we attempted reprogramming with only *OCT4* and *SOX2* (**Fig. 4b**).

However, an inhibitor of the histone methyltransferase DOT1L (iDOT1L) synergized *OCT4*, *SOX2* and DAPT to elevate the rate of iPSC generation by tenfold over the rate with *OCT4*, *SOX2* and DAPT alone, making it even more efficient than four-factor reprogramming either with or without DAPT (**Fig. 4b**). The *OCT4*+ *SOX2*+ DAPT+ iDOT1L colonies could be readily expanded and maintained NANOG and TRA-1-81 expression (**Fig. 4c**). These data indicate that Notch inhibition is a potent enhancer of reprogramming in keratinocytes that can synergize with chromatin-modifying compounds to induce pluripotency at a high efficiency with only *OCT4* and *SOX2*.

Notch inhibition does not compromise p53 activity

Previous studies of p53 and p21 in reprogramming have suggested that ectopic overexpression of reprogramming transcription factors can activate p53, which then induces either apoptosis or the expression of p21, thus inhibiting reprogramming[3,6]. Because suppression of the p53 pathway greatly facilitates iPSC generation, this approach has become an important part of reprogramming methods that reduce or eliminate integrating exogenous transcription factors[3,4]. However, because p53 inhibition allows the accumulation of

genetic mutations during reprogramming[8], alternative approaches for increasing reprogramming efficiencies would be desirable. We therefore next asked whether Notch inhibition promotes reprogramming through a p53-dependent or p53-independent pathway by analyzing the effects of DAPT and DBZ treatment on p53 and its target genes. First, we confirmed the finding that transduction with the iPSC reprogramming factors stimulated p53 activity (**Fig. 5a**). Chemical inhibition of Notch signaling in both human and mouse keratinocytes did not reduce the expression of p53 at the protein or mRNA level either before or after transduction with the reprogramming factors (**Fig. 5b,c** and **Supplementary Fig. 5a,b**). Moreover, transcriptional analysis of DAPT-treated human and mouse keratinocytes revealed that the mRNA levels of the p53 target genes *Tnfrsf10b* (also known as *Dr5*), *Bbc3* (also known as *Puma*) and *Fas* were not decreased (**Fig. 5c** and **Supplementary Fig. 5a,b**), supporting the notion that p53 activity was not suppressed by Notch inhibition.

To further confirm that DAPT treatment did not suppress p53 activity, we performed reprogramming experiments with and without DAPT after UV irradiation. UV exposure causes DNA damage, which in turn reduces reprogramming efficiencies by inducing p53-dependent apoptosis[8]. However, p53-deficient cells are resistant to the negative effects of UV irradiation on reprogramming[8]. Therefore, if p53 activity was maintained in DAPT-treated cultures, then we would expect a sharp decrease in reprogramming efficiency after UV irradiation. As a control for p53 deficiency, we performed four-factor reprogramming with or without UV irradiation using keratinocytes in which we overexpressed a dominant-negative form of p53 (p53DD)[3] that suppressed p53 activity, as evidenced by a decrease in the expression levels of p53-dependent target genes (**Supplementary Fig. 5c**). As expected, UV exposure did not affect the rate of iPSC generation when p53DD was expressed, functionally demonstrating that p53 activity was indeed impaired (**Fig. 5d**). In contrast, in the absence of p53DD overexpression, UV exposure sharply reduced the number of iPSCs generated in DMSO-treated cultures (**Fig. 5d**). Similarly, UV irradiation severely diminished the number of iPSC colonies in DAPT-treated cultures, again suggesting that Notch inhibition does not suppress p53 activity during reprogramming (**Fig. 5d**).

Although the difference in reprogramming efficiency in p53-deficient versus DAPT-treated keratinocytes was clearly evident when UV irradiation was used to induce DNA damage, we next determined whether DNA damage was measurably influenced by DAPT treatment under normal reprogramming conditions. To test this, we quantified phosphorylated histone H2AX (γH2AX) expression in four-factor-transduced human keratinocytes treated with DAPT, p53DD or p53 shRNA. Histone H2AX becomes phosphorylated in response to double-stranded DNA breaks, making it a reliable marker of DNA damage[8]. Pan-nuclear γH2AX expression results from replication-induced damage and could indicate insults sustained during reprogramming[8]. We found that 10 d after transduction, pan-nuclear γH2AX staining was greatly elevated in cultures treated with p53DD or p53 shRNA, which is consistent with a previous study in which elevated rates of DNA damage were observed in p53-deficient cells during reprogramming and in the resulting iPSCs[8] (**Fig. 5e** and **Supplementary Fig. 5d–f**). The DAPT-treated cells, however, maintained low cell numbers with pan-nuclear γH2AX expression that were similar to numbers in the control cultures (**Fig. 5e** and **Supplementary Fig. 5f**). These results suggest that, in contrast to p53 deficiency, DAPT treatment did not promote the survival and reprogramming of cells with DNA damage.

To confirm that Notch inhibition does not prevent the apoptosis of compromised cells during reprogramming, we measured the fraction of TUNEL-positive nuclei in DAPT-treated cultures. Despite high rates of DNA damage in the p53-deficient reprogramming cultures, the percentage of TUNEL-positive nuclei was greatly reduced compared to the percentage in a wild-type control, indicating that inactivation of p53 permitted the survival of cells with compromised genomes (**Fig. 5f**). In contrast, the percentage of TUNEL-positive cells was not reduced after DAPT treatment (**Fig. 5f**).

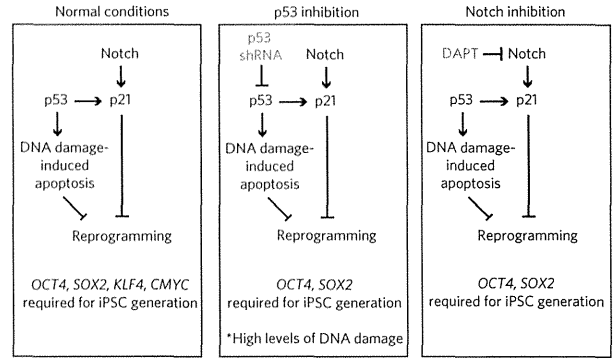

Figure 6 | Model of iPSC generation from human keratinocytes. Notch inhibition allows the production of safer oncogene-free iPSCs by suppressing p21 in a p53-independent manner.

To determine whether DAPT enabled the efficient generation of iPSCs that displayed improved genomic integrity relative to their counterparts made through p53 suppression, we measured the copy number variation in iPSC lines made with DAPT or p53DD. Consistent with the γH2AX and TUNEL staining results, we found that iPSC lines derived in the presence of p53DD had an average of four indels per line, whereas iPSCs derived with a control GFP vector or 10 μm DAPT contained only 1 or 0.5 indels per line, respectively (**Fig. 5g** and **Supplementary Fig. 6**). Together, these experiments show that DNA damage is present during normal reprogramming conditions and that inhibition of p53 allows cells with damaged genomic material to persist. In contrast, Notch inhibition enhances reprogramming without compromising genomic integrity or promoting the survival of iPSCs that have undergone DNA damage.

DISCUSSION

In summary, our findings suggest that signaling through the Notch pathway is a major impediment to the early stages of the reprogramming of both mouse and human keratinocytes into iPSCs (**Fig. 6**). Notably, the mechanism by which Notch signaling most likely inhibits reprogramming of mouse and human cells is by activating p21 independently of p53. Consistent with this hypothesis, treatment of reprogramming cultures with the γ-secretase inhibitors DAPT and DBZ reduced the levels of intracellular Notch and increased colony-forming potential, leading to an increase in the rate of iPSC formation. Suppression of p21 expression by siRNA and shRNA was sufficient to replace Notch inhibition in reprogramming, and exogenous p21 blocked the beneficial effects of DAPT. Notably, the resulting improvement in reprogramming activity did not come at the expense of a reduction in p53 activity or increased genomic instability (**Fig. 6**).

Our findings have immediate and practical ramifications for the improved production of patient-specific human iPSCs. When taken together, our studies show that through pharmacological inhibition of NOTCH, it is routinely possible to produce human iPSCs with only *OCT4* and *SOX2*, rendering *CMYC* and *KLF4* dispensable and thereby reducing the oncogenic potential of the resulting cells. Furthermore, our findings enabled *CMYC*- and *KLF4*-free iPSC production without inhibition of p53 or its target genes involved in apoptosis, allowing proapoptotic pathways that ensure genomic integrity to be engaged[8,10,11]. Thus, in this approach, the production

of oncogene-free iPSC lines does not come at the expense of an increase in mutational load[8,10,11,45].

Studies using nuclear transplantation and defined transcription factors have shown that nuclei become less amenable to reprogramming as they advance developmentally[24–26]. Our study demonstrates that intercellular communication in somatic cultures can cause them to differentiate and lose their reprogramming potential but with small-molecule treatment, it is possible to force them to remain in an undifferentiated, highly reprogrammable state. This approach synergized potently with chemical inactivation of the histone H3 methyltransferase DOT1L, allowing two-factor reprogramming at higher efficiency than with four transcription factors. This indicates that although histone methyltransferase inhibition had almost no effect on the reprogramming of differentiated keratinocytes, it had a profound ability to enhance the reprogramming of undifferentiated keratinocytes. Thus, somatic cells at different developmental stages respond differentially to chromatin-modifying signals during reprogramming. The combined chemical inhibition of NOTCH and DOT1L provides a new approach for boosting the reprogramming potential of keratinocytes and is an attractive starting point for the identification of a small-molecule reprogramming cocktail for human cells.

Accession numbers. Gene Expression Omnibus. Microarray data have been submitted to the GEO repository with accession number GSE35090.

Received 24 September 2013; accepted 13 May 2014; published online 22 June 2014; corrected after print 29 July 2014 and 14 August 2014

METHODS

Methods and any associated references are available in the online version of the paper.

References

1. Aoi, T. *et al.* Generation of pluripotent stem cells from adult mouse liver and stomach cells. *Science* **321**, 699–702 (2008).
2. Nakagawa, M. *et al.* Generation of induced pluripotent stem cells without Myc from mouse and human fibroblasts. *Nat. Biotechnol.* **26**, 101–106 (2008).
3. Kawamura, T. *et al.* Linking the p53 tumour suppressor pathway to somatic cell reprogramming. *Nature* **460**, 1140–1144 (2009).
4. Okita, K. *et al.* A more efficient method to generate integration-free human iPS cells. *Nat. Methods* **8**, 409–412 (2011).
5. Son, M.J. *et al.* Nicotinamide overcomes pluripotency deficits and reprogramming barriers. *Stem Cells* **31**, 1121–1135 (2013).
6. Hong, H. *et al.* Suppression of induced pluripotent stem cell generation by the p53-p21 pathway. *Nature* **460**, 1132–1135 (2009).
7. Utikal, J. *et al.* Immortalization eliminates a roadblock during cellular reprogramming into iPS cells. *Nature* **460**, 1145–1148 (2009).
8. Marión, R.M. *et al.* A p53-mediated DNA damage response limits reprogramming to ensure iPS cell genomic integrity. *Nature* **460**, 1149–1153 (2009).
9. Li, H. *et al.* The Ink4/Arf locus is a barrier for iPS cell reprogramming. *Nature* **460**, 1136–1139 (2009).
10. Li, Y. *et al.* The p53-PUMA axis suppresses iPSC generation. *Nat Commun.* **4**, 2174 (2013).
11. Lake, B.B. *et al.* Context-dependent enhancement of induced pluripotent stem cell reprogramming by silencing Puma. *Stem Cells* **30**, 888–897 (2012).
12. Guo, S. *et al.* Nonstochastic reprogramming from a privileged somatic cell state. *Cell* **156**, 649–662 (2014).
13. Lee, Y.L. *et al.* Sirtuin 1 facilitates generation of induced pluripotent stem cells from mouse embryonic fibroblasts through the miR-34a and p53 pathways. *PLoS ONE* **7**, e45633 (2012).
14. Brosh, R. *et al.* p53 counteracts reprogramming by inhibiting mesenchymal-to-epithelial transition. *Cell Death Differ.* **20**, 312–320 (2013).
15. Ye, D. *et al.* MiR-138 promotes induced pluripotent stem cell generation through the regulation of the p53 signaling. *Stem Cells* **30**, 1645–1654 (2012).
16. Wang, J. *et al.* p53-facilitated miR-199a-3p regulates somatic cell reprogramming. *Stem Cells* **30**, 1405–1413 (2012).
17. Zhu, S. *et al.* Reprogramming of human primary somatic cells by OCT4 and chemical compounds. *Cell Stem Cell* **7**, 651–655 (2010).
18. Silva, J. *et al.* Promotion of reprogramming to ground state pluripotency by signal inhibition. *PLoS Biol.* **6**, e253 (2008).
19. Ichida, J.K. *et al.* A small-molecule inhibitor of Tgf-β signaling replaces *Sox2* in reprogramming by inducing *Nanog*. *Cell Stem Cell* **5**, 491–503 (2009).
20. Hou, P. *et al.* Pluripotent stem cells induced from mouse somatic cells by small-molecule compounds. *Science* **341**, 651–654 (2013).
21. Huangfu, D. *et al.* Induction of pluripotent stem cells by defined factors is greatly improved by small-molecule compounds. *Nat. Biotechnol.* **26**, 795–797 (2008).
22. Federation, A.J., Bradner, J.E. & Meissner, A. The use of small molecules in somatic-cell reprogramming. *Trends Cell Biol.* **24**, 179–187 (2014).
23. Amabile, G. & Meissner, A. Induced pluripotent stem cells: current progress and potential for regenerative medicine. *Trends Mol. Med.* **15**, 59–68 (2009).
24. Eminli, S. *et al.* Differentiation stage determines potential of hematopoietic cells for reprogramming into induced pluripotent stem cells. *Nat. Genet.* **41**, 968–976 (2009).
25. Gurdon, J.B. The developmental capacity of nuclei taken from intestinal epithelium cells of feeding tadpoles. *J. Embryol. Exp. Morphol.* **10**, 622–640 (1962).
26. Li, J., Greco, V., Guasch, G., Fuchs, E. & Mombaerts, P. Mice cloned from skin cells. *Proc. Natl. Acad. Sci. USA* **104**, 2738–2743 (2007).
27. Artavanis-Tsakonas, S. & Muskavitch, M.A. Notch: the past, the present, and the future. *Curr. Top. Dev. Biol.* **92**, 1–29 (2010).
28. Bray, S.J. Notch signalling: a simple pathway becomes complex. *Nat. Rev. Mol. Cell Biol.* **7**, 678–689 (2006).
29. Topley, G.I., Okuyama, R., Gonzales, J.G., Conti, C. & Dotto, G.P. $p21^{WAF1/Cip1}$ functions as a suppressor of malignant skin tumor formation and a determinant of keratinocyte stem-cell potential. *Proc. Natl. Acad. Sci. USA* **96**, 9089–9094 (1999).
30. Missero, C., Di Cunto, F., Kiyokawa, H., Koff, A. & Dotto, G.P. The absence of $p21^{Cip1/WAF1}$ alters keratinocyte growth and differentiation and promotes ras-tumor progression. *Genes Dev.* **10**, 3065–3075 (1996).
31. Aasen, T. & Belmonte, J.C. Isolation and cultivation of human keratinocytes from skin or plucked hair for the generation of induced pluripotent stem cells. *Nat. Protoc.* **5**, 371–382 (2010).
32. Aasen, T. *et al.* Efficient and rapid generation of induced pluripotent stem cells from human keratinocytes. *Nat. Biotechnol.* **26**, 1276–1284 (2008).
33. Blanpain, C., Lowry, W.E., Pasolli, H.A. & Fuchs, E. Canonical notch signaling functions as a commitment switch in the epidermal lineage. *Genes Dev.* **20**, 3022–3035 (2006).
34. Bock, C. *et al.* Reference maps of human ES and iPS cell variation enable high-throughput characterization of pluripotent cell lines. *Cell* **144**, 439–452 (2011).
35. Fuwa, H. *et al.* Divergent synthesis of multifunctional molecular probes to elucidate the enzyme specificity of dipeptidic γ-secretase inhibitors. *ACS Chem. Biol.* **2**, 408–418 (2007).
36. Nam, Y., Sliz, P., Song, L., Aster, J.C. & Blacklow, S.C. Structural basis for cooperativity in recruitment of MAML coactivators to Notch transcription complexes. *Cell* **124**, 973–983 (2006).
37. Nam, Y., Weng, A.P., Aster, J.C. & Blacklow, S.C. Structural requirements for assembly of the CSL.Intracellular Notch1.Mastermind-like 1 transcriptional activation complex. *J. Biol. Chem.* **278**, 21232–21239 (2003).
38. Lefort, K. & Dotto, G.P. Notch signaling in the integrated control of keratinocyte growth/differentiation and tumor suppression. *Semin. Cancer Biol.* **14**, 374–386 (2004).
39. Jones, P.H. & Watt, F.M. Separation of human epidermal stem cells from transit amplifying cells on the basis of differences in integrin function and expression. *Cell* **73**, 713–724 (1993).
40. Kavian, N. *et al.* Targeting ADAM-17/notch signaling abrogates the development of systemic sclerosis in a murine model. *Arthritis Rheum.* **62**, 3477–3487 (2010).
41. Allen, A.S. *et al.* *De novo* mutations in epileptic encephalopathies. *Nature* **501**, 217–221 (2013).
42. Huangfu, D. *et al.* Induction of pluripotent stem cells from primary human fibroblasts with only Oct4 and Sox2. *Nat. Biotechnol.* **26**, 1269–1275 (2008).
43. Mikkelsen, T.S. *et al.* Dissecting direct reprogramming through integrative genomic analysis. *Nature* **454**, 49–55 (2008).
44. Onder, T.T. *et al.* Chromatin-modifying enzymes as modulators of reprogramming. *Nature* **483**, 598–602 (2012).
45. Gore, A. *et al.* Somatic coding mutations in human induced pluripotent stem cells. *Nature* **471**, 63–67 (2011).

Acknowledgments

The authors would like to thank E. Son for assistance with microarray data analysis, S. Sato for assistance with chimera experiments, E. Kiskinis for assistance with nanostring analysis and K. Koszka and M. Yamaki for assistance with teratoma experiments. The authors are grateful for the financial support that made this work possible. K.E. was supported by US National Institutes of Health (NIH)